Asymmetric Hurricane Boundary Layer Structure during Storm Decay. Part I: Formation of Descending Inflow

KYLE AHERN,[a] ROBERT E. HART,[a] AND MARK A. BOURASSA[b]

[a] *Florida State University, Tallahassee, Florida*
[b] *Center for Ocean–Atmospheric Prediction Studies, Tallahassee, Florida*

(Manuscript received 22 February 2021, in final form 3 September 2021)

ABSTRACT: In this first part of a two-part study, the three-dimensional structure of the inner-core boundary layer (BL) is investigated in a full-physics simulation of Hurricane Irma (2017). The BL structure is highlighted during periods of intensity change, with focus on features and mechanisms associated with storm decay. The azimuthal structure of the BL is shown to be linked to the vertical wind shear and storm motion. The BL inflow becomes more asymmetric under increased shear. As BL inflow asymmetry amplifies, asymmetries in the low-level primary circulation and thermodynamic structure develop. A mechanism is identified to explain the onset of pronounced structural asymmetries in coincidence with external forcing (e.g., through shear) that would amplify BL inflow along limited azimuth. The mechanism assumes enhanced advection of absolute angular momentum along the path of the amplified inflow (e.g., amplified downshear), which results in local spinup of the vortex and development of strong supergradient flow downwind and along the BL top. The associated agradient force results in the outward acceleration of air immediately above the BL inflow, affecting fields including divergence, vertical motion, entropy advection, and inertial stability. In this simulation, descending inflow in coincidence with amplified shear is identified as the conduit through which low-entropy air enters the inner-core BL, thereby hampering convection downwind and resulting in storm decay.

SIGNIFICANCE STATEMENT: This is the first part of a two-part study that uses simulations to analyze the cylindrical structure of the lowest 2.5 km of the atmosphere in two major hurricanes: Hurricane Irma in 2017 and Hurricane Earl in 2010. The structure at times when these hurricanes were weakening is highlighted. During those times, the wind and thermal fields had more-variable azimuthal structure, which was linked to the state of the environment that contained the hurricane. The research finds that these azimuthal structures could be physically linked to how the studied hurricanes weaken, and it provides motivation for considering the lower-atmospheric azimuthal structure of hurricanes when analyzing their intensities and changes in their intensities.

KEYWORDS: Advection; Asymmetry; Momentum; Boundary layer; Hurricanes/typhoons; Tropical cyclones

1. Introduction

As part of a continued venture to improve forecasts of tropical cyclones (TCs), recent research has focused on complex TC inner-core structure. Interior dynamics of TCs have been highlighted in examinations of storm evolution, particularly in relation to intensity and vortex structure. Convection and boundary layer (BL) inflow, which may project onto the system-scale secondary circulation, are frequent focal points of TC intensity research. In a mature hurricane, the BL is typically associated with subgradient wind and radial inflow as a result of frictional dissipation, except in the inner core where supergradient winds may be present (Ooyama 1969; Smith et al. 2009). The BL inflow, which picks up internal and latent energy via surface turbulent fluxes along its path, converges and ascends typically near the eyewall, possibly as the root of deep convection. The properties of BL inflow and convergence (e.g., location, magnitude, and spatial extent) evolve over time, dependent on factors like primary vortex structure, environmental shear, storm motion, and proximity to land (Barnes and Dolling 2013; Williams 2019). As changes in BL structure are likely to affect inner-core convection to some degree, such changes can also impact storm intensity. Owing to the TC BL's importance and dynamical complexity, endeavors to further understand the BL's role in TC intensity continue. How the TC and its BL evolve over time in conjunction with changes in TC structure and intensity are of particular interest.

Prior observational and modeling studies have shown that the frictional inflow layer, which could be regarded as the kinematic boundary layer, is insulated by dry and moist statically stable air near its top (Barnes 2008; Zhang et al. 2011, 2013; Kepert et al. 2016; Ahern et al. 2019). Using global positioning system dropwindsondes from three Atlantic Ocean hurricanes, Barnes (2008) identified positive lapse rates of equivalent potential temperature θ_e near the top of BL inflow, which the the author indicates was the result of frictional inflow undercutting rotational air that interacted with the high-θ_e core. Dropwindsonde compositing studies by Zhang et al. (2011, 2013) and Ahern et al. (2019) found dry statically stable air near the top of BL inflow. Kepert et al. (2016) deduced in their modeling study that the dry static stability is due to evaporative cooling near

Ahern's current affiliations: NOAA/AOML/Hurricane Research Division and Cooperative Institute for Marine and Atmospheric Studies, University of Miami, Miami, Florida.

Corresponding author: Kyle Ahern, kyle.ahern@noaa.gov

DOI: 10.1175/MWR-D-21-0030.1

the BL top from rainfall, as well as vertically differentiating radial advection of potential temperature (weakening cold-air advection with height near the BL top in tandem with weakening inflow with height). Over warm waters, entropy accumulates in an insulated BL via heat and moisture fluxes, and the convergence and ascent of consequently high-entropy air could lead to deep convection.

Via mass continuity, convergence through the BL is associated with ascent at the BL top (Kepert 2013). Given that inner-core BL air is often entropy-rich when it converges and ascends into the free atmosphere, recent research has concluded that areas of BL convergence are favorable for developing deep convection (Rogers et al. 2013, 2015, 2016; Hazelton et al. 2017a; Zhang et al. 2017). Various types of inner-core convection, such as convective bursts, hot towers, and vortical hot towers, have been tied to TC genesis and intensification (Hendricks et al. 2004; Montgomery et al. 2006; Nolan et al. 2007; Fang and Zhang 2011; Nguyen and Molinari 2015; Hazelton et al. 2017b; Chen et al. 2018a). Several studies (e.g., Shapiro and Willoughby 1982; Pendergrass and Willoughby 2009; Vigh and Schubert 2009; Rogers et al. 2013; Chen et al. 2018b) have examined links between the radial position of deep convection and TC intensity, finding that convection—and the diabatic heating therefrom—near or within the radius of maximum winds (RMW) is conducive for RMW contraction and intensification. Convection inward of the RMW might also lead to TC intensification via a BL spinup mechanism (Smith and Montgomery 2016): The inward advection of absolute angular momentum M in the BL can cause the flow to become supergradient at sufficiently small radii, and vertical advection of this momentum in the inner core (i.e., through BL convergence) could spin up tangential winds in the free atmosphere where winds are closer to gradient-wind balance. Regardless of the mechanisms directly responsible, past work generally agrees that deep convection concentrated close to the RMW is typically associated with an intensifying TC, although other factors (e.g., oceanic heat content, maximum potential intensity, ventilation) can also be just as critical to intensification (Emanuel 1986; Zhang and Emanuel 2016; Chavas 2017). In simulations of the TC BL, Kepert (2017) found that the distance of the eyewall's frictional updraft from the RMW scales with $-u_{10}/I$, where u_{10} is the 10-m inflow and I is the inertial stability. Because the inertial stability is a function of the radial profile of M and conceptually represents a resistance to radial displacement, Kepert's study exemplifies how the primary and secondary circulations can cooperatively establish the frictional updraft. Further, note that frictional updrafts need not be confined to the vicinity of the RMW, and they could potentially mark the formative region for a secondary eyewall [this prospect is examined in Ahern et al. (2021, manuscript submitted to *Mon. Wea. Rev.*), hereinafter Part II].

While the radial distribution of BL convergence and convection are apparently consequential to TC intensity and evolution, a TC's azimuthal structure is also important to consider. TC structure can be markedly asymmetric, complicating the intensity problem and borne of factors like environmental shear or vortex tilt (Black et al. 2002; Corbosiero and Molinari 2002; Riemer et al. 2010; Reasor et al. 2013; Rogers et al. 2013; DeHart et al. 2014; Gu et al. 2016; Hazelton et al. 2017a; Nguyen et al. 2017; Rios-Berrios et al. 2018; Ryglicki et al. 2018), translation of the TC (Shapiro 1983; Kepert 2001; Kepert and Wang 2001), and proximity to land (Kepert 2006; Williams 2019). Vertical shear is associated with horizontal temperature gradients and tilting of the vortex that may affect the horizontal distributions of convection, rainfall, and downdrafts, which affect the structure of the secondary circulation (Corbosiero and Molinari 2002; Rios-Berrios et al. 2018; Ryglicki et al. 2018). Riemer et al. (2010) examined TC–shear interactions in a set of idealized experiments, finding that shear can affect the TC energy cycle by flushing the BL with low-entropy air via asymmetric downdrafts; low-entropy BL air parcels can reach the eyewall without recovering their entropy via air–sea fluxes, thereby impacting TC intensity. Aside from the effects of shear, the superposition of a motion vector onto a symmetric cyclone amplifies the Earth-relative flow to the right of motion in the Northern Hemisphere (and vice versa left of motion), and it is accompanied by asymmetry in frictional forcing that is roughly proportional to the square of the wind speed (Shapiro 1983). Similarly, the proximity of a TC to land can induce asymmetry, as momentum would be dissipated more effectively over the relatively rough land surface, thereby affecting agradient forcing (Kepert 2006; Barnes and Dolling 2013; Williams 2019).

It is likely that multiple factors act in concert to modulate the azimuthal structure of the TC, interfering with one another constructively or destructively (Sitkowski and Barnes 2009; Barnes and Dolling 2013). Corbosiero and Molinari (2003) examined the azimuthal distribution of lightning in TCs with relation to both environmental shear and TC motion, and concluded that inner-core convection tended to concentrate downshear and downshear-left, and also downstream of a moving TC. However, Corbosiero and Molinari found that the horizontal distribution of convection was dominated by shear, as the effect of asymmetric friction associated with TC motion (Shapiro 1983) did not emerge when both shear and motion were considered. Shear was also found to be the dominant factor over TC motion in distributions of rainfall (Chen et al. 2006), although these studies clarified that TC motion could be an important factor for the distribution of convection and rainfall under weak shear. Furthermore, while these studies noted that TC motion is generally not the dominant factor in distributions of convection, that does not necessarily indicate that TC motion has no meaningful role in TC structure. For instance, Rappin and Nolan (2012) found in their examinations of TC cyclogenesis that the orientation of the mean surface wind in a vortex with relation to the shear affects the spatial distribution of dry air as well as convection and the vortex tilt, with antiparallel configurations resulting in weaker vortex tilt.

Asymmetric convection and rainfall are often related to asymmetries in BL structure, especially asymmetries in radial velocity and convergence. Inflow in the inner-core BL has been found to be amplified downshear (Zhang et al. 2013) and to the front or front-right of a translating TC (Shapiro 1983; Kepert 2001; Barnes and Dolling 2013), with convergence shifted cyclonically downwind. Alongside the effect on convergence, asymmetric inflow would also affect advection, which is expected

to be a critical avenue through which the azimuthal structure is affected for other low-level fields (e.g., vertical and horizontal momentum, entropy, agradient force). Essentially, the amplification of asymmetry in the low-level radial flow—for instance, because of shear, motion, or tilt—can have a cascading effect. Studies of the azimuthal distribution of convection and rainfall about environmental shear (e.g., Rogers et al. 2013; DeHart et al. 2014; Hazelton et al. 2017a; Zhang and Rogers 2019) depict examples of such asymmetry cascading: low-level convergence is amplified downshear in tandem with enhanced inflow, resulting in convective initiation there; rainfall and convective downdrafts occur downwind, to the left of shear in the Northern Hemisphere.

In this two-part study, full-physics simulations are used to analyze 3D kinematic and thermodynamic BL structure, all in relation to changes in intensity, shear, and TC motion. Results are presented from simulations of Hurricanes Irma (2017) and Earl (2010), with a focus on asymmetric BL structure coincident with vortex decay. At the outset, these two cases were chosen for their comparable maximum TC intensity and differing environmental influences, namely, shear and storm motion (or, by proxy, the steering flow). The objective of this work is to examine how deep-layer shear and TC motion relate to BL structure and evolution in mature hurricanes, and how the BL as modulated by shear and TC motion affects vortex intensity and structure. Note that the layer of shear that most effectively impacts TC structure is variable from case to case and could be linked to motion (Zeng et al. 2010). Given that the cases to be analyzed will be intense hurricanes, shear computed through a deep tropospheric layer is generally used. The impacts of shear and TC motion on the BL's azimuthal structure are suspected to have played an important role in the weakening of both simulated TCs. In these cases, it is found that asymmetrically amplified inflow and M advection associated with shear and TC motion led to agradient forcing asymmetry, which in turn affected the low-level primary and secondary circulations to the detriment of TC intensity.

This first part will focus on a simulation of Hurricane Irma. The modeling configuration used in both simulations is outlined in the following section. In section 3, an analysis and interpretation of Hurricane Irma's simulated structure is presented, focusing on azimuth-mean and shear-relative BL structure during periods of intensification and weakening that followed one another. Section 4 details the evolution of asymmetric inflow and descent of low-entropy air into Irma's BL, which is associated with a TC weakening phase. In section 5, momentum budgets are analyzed to discuss avenues through which asymmetries associated with Irma's weakening may have developed, which will be revisited in a study of Hurricane Earl in Part II. A concluding summary and discussion of Irma's simulated evolution are given in section 6.

2. Method

a. Model configuration

The vortex-following configuration of the advanced research version of the Weather Research and Forecasting Model (WRF-ARW, version 3.9; Skamarock et al. 2008) is employed for the full-physics simulations. Four domains are set, which telescope into one another with increasing horizontal resolution: 36-km resolution in the parent (first) domain, 12-km resolution in the second domain, 4-km resolution in the third domain, and 1.333-km resolution in the innermost (fourth) domain. Domain boundaries at initialization time for Hurricane Irma are shown in Fig. 1. Domains use progressively smaller time steps with increasing spatial resolution: 108 s in the first domain, 36 s in the second, 12 s in the third, and 4 s in the fourth. The domains are allowed to feed back onto each other through two-way interaction. Unless otherwise stated, all plots and analysis are based on results from the innermost domain, which has a 15-min output frequency. For Hurricane Irma, the period between 0000 UTC 3 September and 0000 UTC 11 September is simulated.

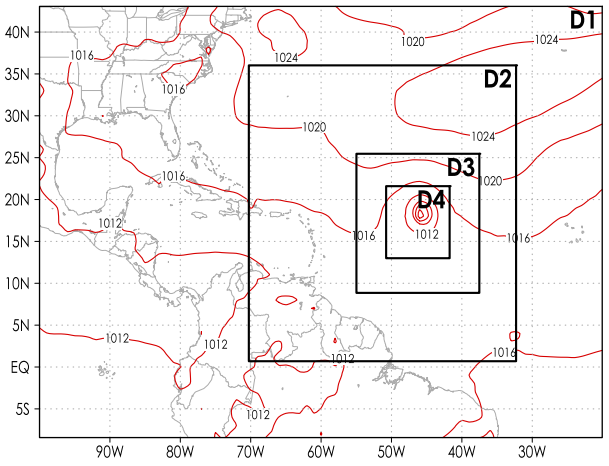

FIG. 1. Map of the four domains set at initialization time (0000 UTC 3 Sep 2017) for the simulation of Hurricane Irma, with each domain represented by a black-outlined box and labeled by domain number. Red contours are mean sea level pressure (hPa, with 4-hPa interval) from NCEP FNL Operational Global Analysis data (NCEP 2000).

The model is provided initial and parent-domain boundary conditions through 6-hourly National Centers for Environmental Prediction (NCEP) Final (FNL) Operational Model Global Tropospheric Analysis data. NCEP FNL data have a 1° spatial resolution. The simulations use a model top of 20 hPa with 71 terrain-following vertical levels. Vertical levels are packed most densely in the lower troposphere, with 13 below and including the level at $z = 2.57$ km, 9 levels below $z = 1.5$ km, and a minimum grid spacing of 50 m for the lowest layer. The grid spacing in these lower 13 layers varies from about 50 m at the lowest layer to 420 m at the top. Elsewhere, vertical grid spacing is about 425 m, except near the tropopause at $z \approx 17$ km where a relative minimum of 390 m grid spacing is reached. The innermost nest tracks the vortex using a geopotential minimum at the model level closest to 600 hPa, which effectively follows the TC after model spinup. The third domain moves with the fourth domain, and the second domain moves if the third domain advances within 288 km of the second domain's boundary.

The third and fourth domains are set to resolve convection explicitly, using no cumulus parameterization scheme; the first and second domains use the Kain–Fritsch (Kain 2004) scheme. Morrison double-moment microphysics (Morrison et al. 2009) is used. A recent study by Wu et al. (2021) showed that the median of raindrop sizes produced by the Morrison scheme was larger than was observed in outer rainbands of Typhoon Nida (2016) while the area-averaged liquid water content associated with convective precipitation was less than observed. These biases may influence the distribution and intensity of convective updrafts and downdrafts; in particular, local BL structure may be affected by strong downdrafts that extend into the BL. The revised MM5 surface layer parameterization (Jiménez et al. 2012) is used with modified surface exchange coefficients for momentum and enthalpy for TC applications. The planetary boundary layer is parameterized by the Yonsei University (YSU) scheme (Noh et al. 2003; Hong et al. 2006), which is the default option in the WRF 3.9 tropical physics suite and has seen frequent use in TC experiments, including the "hurricane nature run" (Nolan et al. 2009a,b, 2013; Hazelton et al. 2017a,b). The studies of Hurricane Isabel (2003) by Nolan et al. (2009a,b) indicated that, although YSU produced BL structures that were mostly consistent with observations, there were differences to note, including an RMW that was 10–15 km larger than the 25 km that was observed, stronger BL inflow and overlying outflow, weaker near-surface winds, and weaker radial gradients of moisture. Model physics options are summarized in Table 1. All raw model output is run through WRF-ARW's postprocessing program, ARWpost, to convert the model's terrain-following staggered grid to longitude–latitude–height space, which is analyzed after regridding to TC-centered cylindrical coordinates.

TABLE 1. Shared WRF Model physics specifications for simulations of Hurricanes Irma and Earl.

PBL scheme	Yonsei University (Noh et al. 2003; Hong et al. 2006)
Surface layer	Revised MM5 with TC-modified exchange coefficients (Jiménez et al. 2012)
Land surface	Unified Noah (Tewari et al. 2004)
Cumulus physics	Kain–Fritsch (Kain 2004) for domains 1 and 2; none for domains 3 and 4
Microphysics	Morrison double-moment (Morrison et al. 2009)
Radiation physics	Rapid Radiative Transfer Model for GCMs (RRTMG; Iacono et al. 2008)

b. Analysis details

Most of the analysis utilizes storm-centered, shear-relative, cylindrical coordinates. Closer to the center, tangential and radial velocity fields become increasingly sensitive to the TC's central position. The TC's center at a given time is defined with an iterative method that uses a centroid of pressure (Nguyen et al. 2014) at $z \approx 1.84$ km above ground level. The method requires a first-guess center and environmental pressure p_0. For the first-guess center, the WRF-diagnosed vortex center based on the geopotential minimum near 600 hPa is provided. For p_0, the third domain's nearest-in-time (6-hourly output) mean pressure p within a 10-km-wide annulus centered at $r = 500$ km is used. Ryglicki and Hart (2015) found that using the iterative p-centroid to define the TC's center minimized apparent vortex tilt in hurricanes; because the focus of this work primarily concerns shear and TC motion as opposed to the vortex tilt, the choice of a p-centroid for defining the TC center is suitable. Because most of the kinematic fields examined here are relative to the TC's motion (e.g., storm-relative radial wind), TC zonal and meridional motions are calculated using 6-h time-centered differences of central longitude and latitude, respectively.

The cylindrical grid's azimuthal coordinate is relative to the environmental deep-layer shear, which is defined similar to that in data from the Statistical Hurricane Intensity Prediction Scheme (SHIPS; DeMaria et al. 2005). The shear is calculated by first averaging the horizontal wind over storm-centered, 200–800-km annuli on height surfaces closest to 850 and 200 hPa and then subtracting the ~850-hPa annulus-mean wind from that at ~200 hPa. Because the size of the annulus is too large to calculate shear using data from the innermost domain, winds from the third domain with 6-hourly output are used. The deep-layer shear is interpolated linearly every 15 min between each output from the third domain. For specific parts of the analysis, a local shear metric is also determined, which uses the winds averaged within 200 km of the TC center at the same levels.

Model output is regridded to a cylindrical grid with radius r, shear-relative azimuth λ, and height z following the method outlined in Ahern and Cowan (2018), which minimizes error when transposing geospatial data to a TC-centered grid. For the purposes of calculating derivatives on the cylindrical grid (e.g., for advection), the transposed data are sorted into spatial bins with 2-km radial width and 30° azimuthal resolution. The transposed and derived data are then binned to an analysis grid with 2-km resolution in r and four shear-relative quadrants: downshear-left (DSL), downshear-right (DSR), upshear-left (USL), and upshear-right (USR). The analysis grid shares vertical resolution with the postprocessed geospatial grid.

For this study, measures of TC intensity V_{max} and intensity tendency dV_{max}/dt are necessary. To reduce some of the transience in the intensity metric and thereby reduce the noise in the measure of intensity change, the intensity is defined here as the maximum azimuth-mean, storm-relative tangential wind speed at $z \approx 2.57$ km. This height is chosen to detect intensity because it is outside the highly transient winds closer to the surface, within 1–2 km of the kinematic boundary layer in the analysis, and close to flight level for TC reconnaissance. The RMW is taken as the radius at which V_{max} is detected. The intensity tendency is determined by first applying a time-centered, 3-h box smoother to the V_{max} time series. Next, for a given analysis time, the linear regression of smoothed V_{max} versus time is computed using data from the prior 6 h, the following 6 h, and the analysis time itself (i.e., a 12-h, time-centered linear regression with $N = 49$). The slope of the resulting best-fit line represents dV_{max}/dt. At a given time, the TC is declared to be intensifying if $dV_{max}/dt \geq 20$ kt (24 h)$^{-1}$,

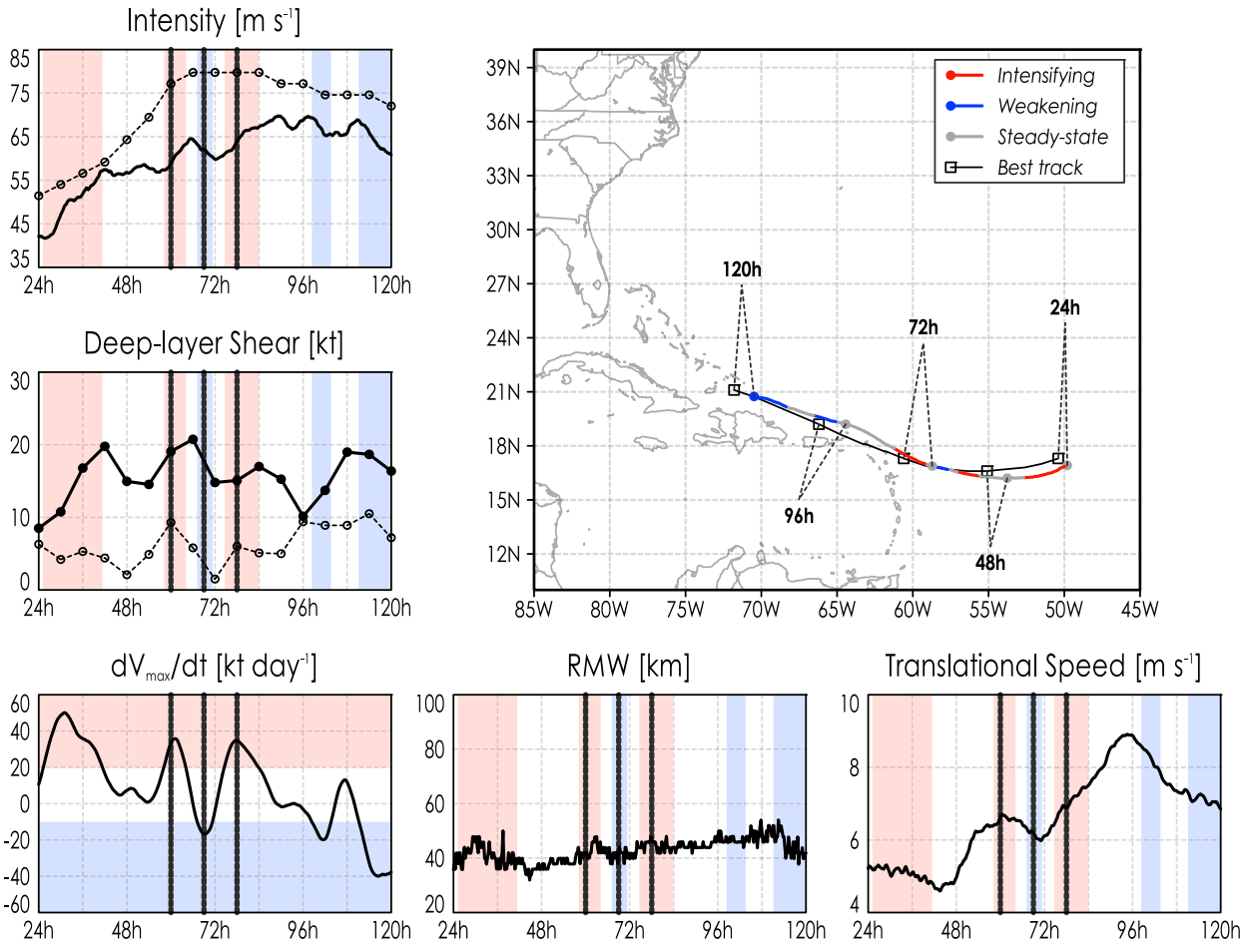

FIG. 2. Hurricane Irma's simulated track and best track (HURDAT2) between 4 and 8 Sep (simulation hours 24–120), with time series of (top left) simulated intensity V_{max} (solid) and best-track intensity (dashed), (middle left) simulated deep-layer shear (solid) and SHIPS deep-layer shear (dashed), (bottom left) intensity tendency dV_{max}/dt, (bottom middle) radius of maximum winds (RMW), and (bottom right) TC translational speed. (top right) Track plot, with the simulated path shaded on the basis of intensification rate as indicated in the plot's legend; the black path follows the best track. Shading in the intensity tendency time series delineates thresholds for intensification (red) and weakening (blue), which is used in all other time series to indicate periods of intensification and weakening. Black vertical lines in time series mark simulation hours 60 (T0), 69 (T+9), and 78 (T+18).

weakening if $dV_{max}/dt < -10\,\text{kt}\,(24\,\text{h})^{-1}$, or steady-state otherwise ($1\,\text{kt} \approx 0.5\,\text{m}\,\text{s}^{-1}$). These thresholds are identical in value to those used in the observational study by Ahern et al. (2019) and are similar to that of Rogers et al. (2013).

For the sake of clarity in describing azimuthal structure, the following terminology is declared for TC-relative positions used in this study explicitly:

- ''downshear'' and ''upshear'' reference positions ahead of and behind the heading of the deep-layer shear, respectively;
- ''downstream'' and ''upstream'' refer to positions ahead of and behind the heading of TC motion, respectively; and
- ''downwind'' and ''upwind'' reference positions ahead of and behind the Earth-relative flow, respectively.

The simulations are allowed a day to evolve and develop vortex structure at model resolution, ignoring the output prior to this spinup time in the analysis. Output analysis is avoided where the inner-core region is likely to be strongly influenced by land, limiting the inclusion of simulation times where a TC is within 160 km of a landmass.

3. Structural analysis of Hurricane Irma

a. General overview

Before the BL structure associated with Hurricane Irma's weakening is examined, a general overview of the simulation is provided. Figure 2 shows Hurricane Irma's simulated track and best track from HURDAT2 (Landsea and Franklin 2013) over four days following the first 24 h of simulation time (i.e., from 4 to 8 September), along with time series of intensity V_{max}, deep-layer shear, intensity tendency dV_{max}/dt, RMW, and storm motion. Irma moved west to west-northwest, tracking north of

the Antilles and following best track closely. The simulation mostly intensified between 24 and 40 h, and then remained in a steady-state period until ~57 h. For the analysis, three periods are closely examined in the 24 h following the aforementioned steady-state period, when the simulation intensified (60 h, which is called T0), weakened (69 h, or T+9), and then intensified once again (78 h, or T+18).[1] From T0 to T+18, the simulated Irma maintained major-hurricane status on the Saffir–Simpson scale, but was consistently weaker than Irma in reality at the same time—best-track intensity was ~80 m s^{-1} for this period. The methods used here to calculate V_{max} differ from that of best track, and the use of azimuthal-mean tangential wind as opposed to a point maximum of total wind result in weaker intensities. Further, the changes in simulated intensity between T0 and T+18 are not present in real data. Although some structural similarities are shown between observations and the simulation, model results here are best interpreted as a realistic forecast of Irma, rather than as a precise case study of Irma as observed.

As Irma intensified at T0, the simulated deep-layer shear had increased to about 19 kt and then to 21 kt 6 h later, just prior to weakening at T+9. Then, 3 h after T+9, the shear weakened to 15 kt and persisted until T+18 as Irma stopped weakening and resumed intensifying. The simulated shear is stronger than Irma's observed shear as reflected by SHIPS data; the SHIPS shear increased to about 9 kt at T0, decreased to about 1 kt by T+12, and increased to about 6 kt at T+18. The discrepancy suggests that the simulation may produce a more asymmetric BL structure relative to reality. However, an observational examination of Irma by Fischer et al. (2020) noted that while SHIPS data indicated shear persistently weaker than 10 kt that would likely preclude substantial convective asymmetries in a mature hurricane, observations depicted such asymmetries with increased rainband activity downshear. Using tail Doppler radar data, they calculated the vertical shear relative to the mean wind at an altitude of 2 km, within 80 km of Irma's center, and between 2- and 9-km heights. The local shear was stronger than the SHIPS shear metrics, with local shear gradually decreasing from ~16 to 12 kt across NOAA WP-3D missions 20170904H2 (2009 UTC 4 September–0321 UTC 5 September), 20170905H1 (0754–1354 UTC 5 September), and 20170905H2 (2015 UTC 5 September–0247 UTC 6 September)—these missions cover the simulation from ~T−16 to T+15. Translational speed followed a similar pattern to shear, being relatively strong near T0 and relatively weak at T+9, but the variations were of lesser magnitude.

The vortex tilt, or the horizontal displacement in the vertical of the vortex center from a reference point, is a metric dependent on the vertical profile of environmental flow acting upon the vortex. The tilt of the vortex has been linked to asymmetries in convection and precipitation, and the timing of changes to intensity has been tied to adjustments or vertical alignments of tilt, particularly in examinations of TCs under moderate vertical shear (e.g., Rios-Berrios et al. 2018; Ryglicki et al. 2018). Vortex tilt is shown in Fig. 3 at T0, T+9, and T+18; the tilt is calculated using the iterative pressure centroid method of Nguyen et al. (2014) to find the TC center at all model levels below z = 13 km, which is compared with the center used for tracking defined in section 2. The vertical profile of horizontal flow acting on a TC also affects measures of shear, as well as TC motion through steering. Hodographs associated with the tilt are also provided in Fig. 3; each hodograph uses winds averaged within 200 km of the TC's tracking center, which is used to establish the local shear every 15 min in section 4. At T0 and T+9, the simulated local background wind below z = 8 km was directed mostly northwestward of Irma, while higher-level winds were directed relatively southward, indicating southward deep-layer shear. From T0 to T+9,

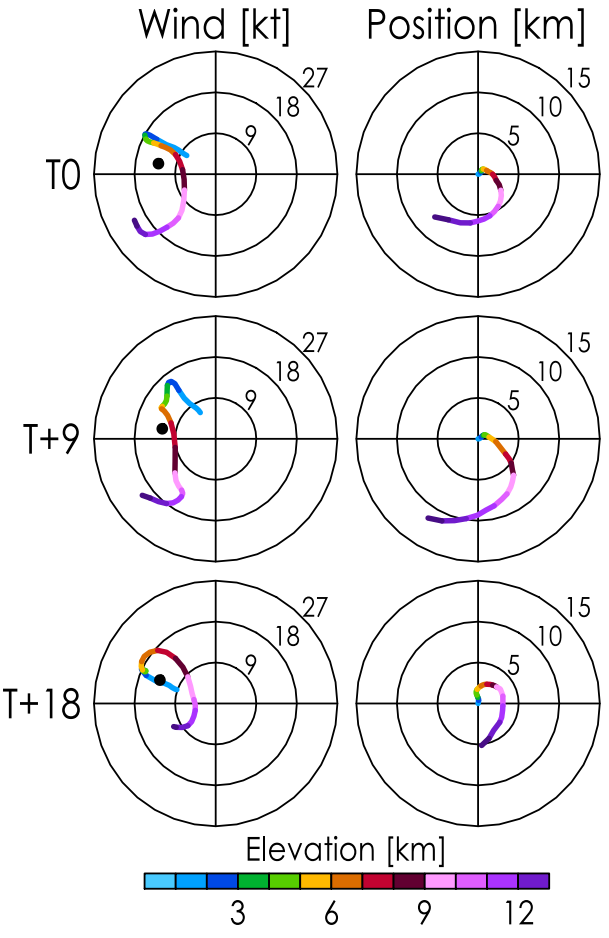

FIG. 3. (left) Hodographs of winds averaged within 200-km radius at (top) T0, (middle) T+9, and (bottom) T+18. (right) The vortex tilt, shown using the pressure centroid position relative to the center taken at $z \approx 1.84$ km, using the iterative method from Nguyen et al. (2014). Profiles are shaded by elevation. The black dot in each hodograph represents the TC motion at the time. Intervals of wind speed or distance are marked at the top-right corner of each concentric circle. The top of the page represents north.

[1] Henceforth, T+X is used to refer to simulation times after T0 (T−X for times before T0), where X is the number of hours separated from T0.

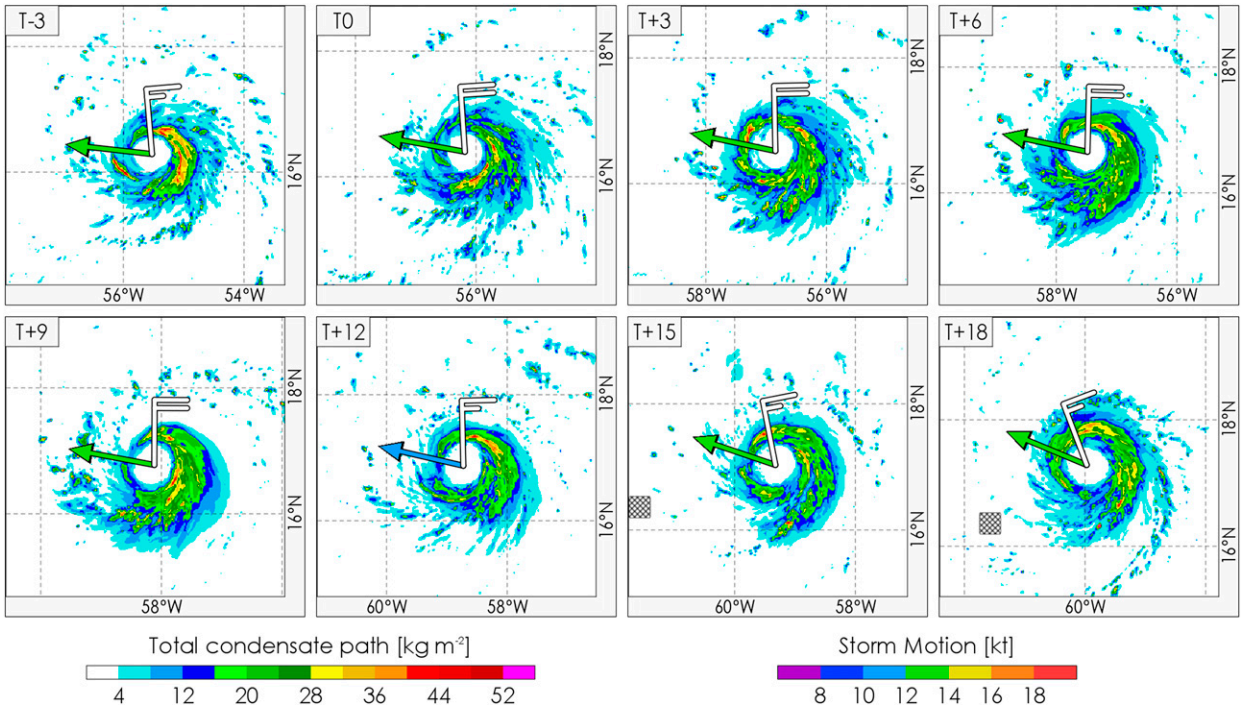

FIG. 4. Snapshots of Hurricane Irma's simulated total condensate path in the troposphere ($kg\,m^{-2}$) every 3 h from T−3 to T+18. Vectors indicate Irma's motion, which are colored by magnitude. Wind barbs represent the environmental deep-layer shear direction and magnitude. Cross-hatched areas represent land in the model.

Irma's tilt below $z = 8$ km increased from about 2.5 km toward the east to about 5 km toward the southeast. Over the same time, Irma's center above $z = 8$ km advanced anticyclonically outward toward the southwest, with the position at $z = 12$ km shifted about 7 km away from the central axis at T0 to about 11 km away at T+9. By T+18, the hodograph became tighter around the west-northwestward storm motion and indicated a more westerly turn of the deep-layer shear from T+9. The tilt at T+18 was also minimized relative to earlier analysis times, with the tilt up to $z = 13$ km reaching 5-km displacement. The shift of the low- to midlevel tilt from T+9 to T+18 is cyclonic and inward from DSL to USL, which Rios-Berrios et al. (2018) noted in their study of moderately sheared, idealized TCs is indicative of humidification of the upshear sector, symmetrization of precipitation, and intensification.

Although the tilt shown in Fig. 3 is referenced later, this work will focus on asymmetries and evolutions as they relate to the motion and shear, so to address how BL structure is modulated by the combination of frictional effects pertaining principally to motion, and large-scale effects pertaining to shear as outlined in the introduction. It will be shown that the amplification of the deep-layer shear during intensification at T0 was associated with asymmetric evolution in Irma's secondary circulation, which set the stage for the weakening phase at T+9 when shear and vortex tilt were relatively large. It is suspected that as shear fell to 15 kt after T+9, asymmetric forcing from the large-scale environment onto Irma's secondary circulation was reduced as indicated by the reduced tilt in Fig. 3, which allowed Irma to axisymmetrize asymmetric features, such as those in precipitation, that developed hours earlier.

To examine the evolution of simulated precipitation, Fig. 4 provides several snapshots of the total condensate path (TCP) at times near the focus periods. Following the formulation for total condensed water of the column used by Ryglicki et al. (2018), TCP is defined as

$$\mathrm{TCP} \equiv \int_0^{z_{\mathrm{trop}}} \rho r_{\mathrm{total}}\, dz\,, \tag{1}$$

where z_{trop} is the tropopause at $z \approx 17$ km, ρ is air density, and r_{total} is the sum of mixing ratios of cloud water, rainwater, ice, snow, and graupel. Between T−3 and T+9, northerly deep-layer shear persisted as Irma moved west-northwestward toward the Lesser Antilles, with the storm motion vector nearly orthogonal and to the right of the shear vector. Over the same time span, relatively high TCP isolated left of shear, while TCP to the right of shear became minimized by T+9, in agreement with precipitation asymmetries expected (Rios-Berrios et al. 2018) with the increased tilt seen at T+9 in Fig. 3. Along with a swath of minimized cloudtop temperatures to the left of shear in simulated infrared imagery (not shown), the TCP evolution from T−3 to T+9 implies that convective activity became more concentrated DSL, with hydrometeors falling out of convection and into the left-of-shear semicircle. As shear weakened and Irma veered slightly northward after T+9, the asymmetry appeared to wrap around the upshear side of Irma as the vortex center aloft shifted cyclonically toward the USL

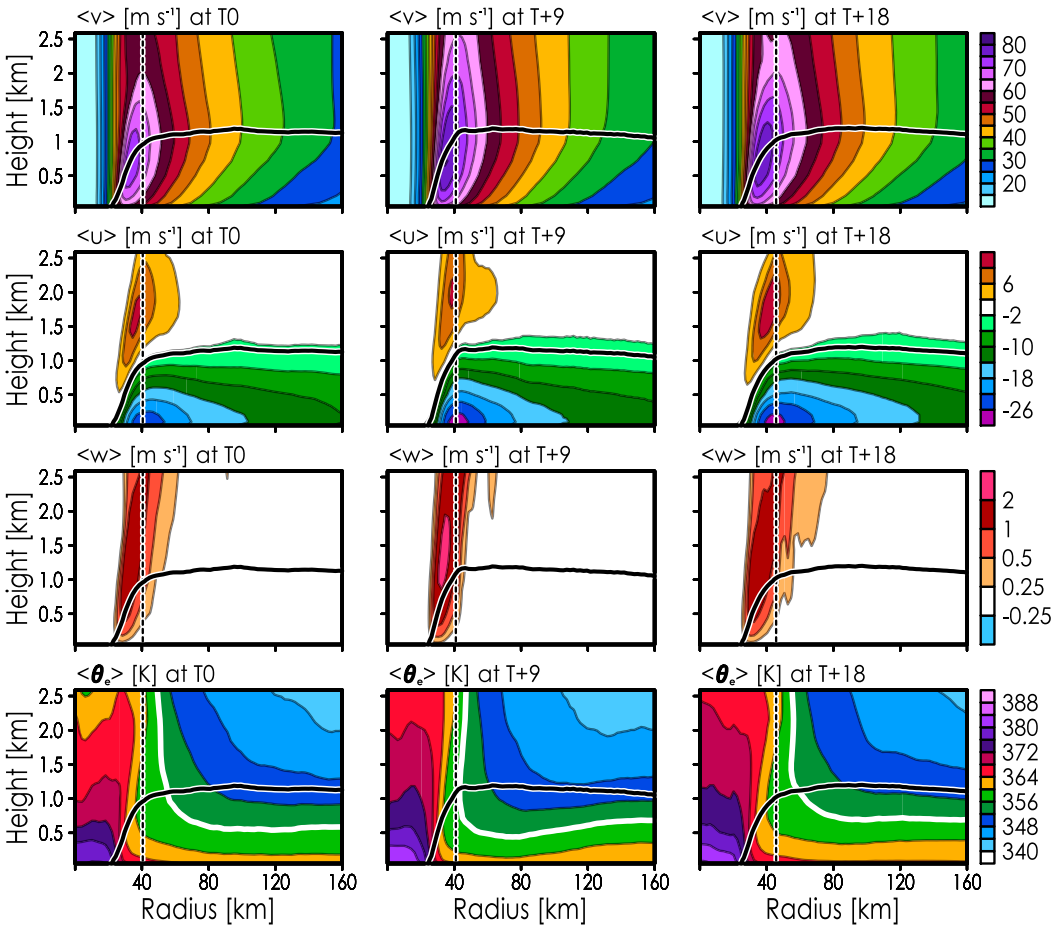

FIG. 5. Radius–height cross sections of azimuth-mean (top) tangential velocity v, (top middle) radial velocity u, (bottom middle) vertical velocity w, and (bottom) equivalent potential temperature θ_e at (left) T0, (center) T+9, and (right) T+18. The vertical dashed line marks the RMW. The thick, solid black line represents the boundary between the kinematic boundary layer and the free atmosphere, which is defined as where $\langle u \rangle$ is 10% of the peak azimuth-mean inflow in the domain. In the $\langle \theta_e \rangle$ plots, the 356-K contour is highlighted in thick white. All fields have been smoothed over 2 h. The scale used for $\langle w \rangle$ is geometric.

quadrant. By T+18, precipitation about Irma's center had a mostly symmetric horizontal distribution, which persisted until moving into proximity to Puerto Rico (not shown). This apparent axisymmetrization occurred as the TC motion became more counteraligned with the shear while the tilt became minimized, as similarly seen in Rappin and Nolan (2012). The convective asymmetry implied in Fig. 4 will be examined after an assessment of the simulation's azimuth-mean BL structure.

b. *Axisymmetric evolution*

For the three focus periods, Fig. 5 shows low-level, radius–height cross sections of azimuth-mean fields of storm-relative tangential velocity v, storm-relative radial velocity u, vertical velocity w, and equivalent potential temperature θ_e. Fields that are "storm relative" are those in which the TC's motion as outlined in section 2 has been subtracted from the horizontal wind field. The formulation in Bolton (1980) is used to determine θ_e, which requires saturation vapor pressure and was calculated following Alduchov and Eskridge (1996). All fields are averaged over a 2-h window centered at the noted time. Azimuth-mean fields are expressed with the variable enclosed in angle brackets (e.g., $\langle u \rangle$ for azimuth-mean u). In radius–height cross sections, the kinematic boundary layer is defined here as the region below $z = 1.5$ km where the azimuth-mean inflow is at least 10% of the peak azimuth-mean inflow, similar to the definition used by Zhang et al. (2011, 2013). For this two-part study, regions outside of the kinematic BL will be regarded as the free atmosphere.

From T0 to T+18, Irma's low-level primary circulation featured a powerful jet region near $r = 40$ km, with the RMW also positioned near $r = 40$ km. The kinematic BL was roughly 1–1.2 km deep outside the RMW, and increasingly shallow with decreasing radius inward of the RMW. In the kinematic BL, tangential velocity had a positive vertical gradient, which is an expected consequence of surface friction. Irma's tangential wind jet deepened and intensified between T0 and T+9, and weakened somewhat between T+9 and T+18. Outside of the volatile winds in the interior, Irma's

azimuthal-mean low-level primary circulation broadened slightly from T0 to T+18.

Irma's low-level secondary circulation had a similarly subtle azimuth-mean evolution between T0 and T+18. Irma's inflow strengthened near the surface between T0 and T+18; peak azimuth-mean inflow near the RMW increased to over 26 m s^{-1} by T+9, and the radial extent of inflow stronger than 14 m s^{-1} increased between T+9 and T+18. Radial outflow persists above the kinematic BL near the RMW, which is representative of inflowing air parcels converging and recoiling after entering the highly inertially stable interior of the vortex. The outflow region broadens slightly from T+9 to T+18 as Irma begins to reintensify. In the mean vertical velocity field, an area of ascent with $\langle w \rangle > 1$ m s^{-1} was consistently along the inner periphery of the RMW, sloping outward with height. The ascent amplified between T0 and T+9, and then weakened between T+9 and T+18. In other words, the peak low-level azimuth-mean ascent in Irma's inner core may have been maximized as Irma weakened at T+9, which defies the conventional perspective that stronger BL convergence and low-level ascent inward of the RMW is generally conducive for hurricane intensification. By T+18, the area of ascent was less radially confined to the RMW, with weak ascent also seen above the BL out to radii of ~70 km.

Azimuth-mean profiles of θ_e provide hints that dry air may have entrained into Irma's BL during vortex decay, providing a possible explanation for Irma's weakening despite an increase in $\langle w \rangle$ between T0 and T+9. At T0 and T+18, surfaces of constant $\langle \theta_e \rangle$ in the kinematic BL were nearly horizontal at outer radii, turning upward and becoming more vertically aligned near the RMW. The high θ_e close to the TC center typifies the warm hurricane eye. Between T0 and T+9, $\langle \theta_e \rangle$ at Irma's center increased in tandem with the increased storm intensity, and BL θ_e-surfaces developed a downward dip between the RMW and a radius of ~120 km. Lower-θ_e air also extended farther inward in the BL at T+9 relative to T0 and T+18. For instance, the 356-K $\langle \theta_e \rangle$ contour began to curve upward just inward of $r = 80$ km at T0, becoming nearly vertical at about $r = 50$ km. At T+9, the same contour curved downward near $r = 120$ km and sharply turned upward at $r \approx 50$ km, becoming nearly vertical at $r \approx 40$ km, indicating that lower-θ_e air had been drawn into the low-level interior.

The differences between azimuth-mean θ_e among T0, T+9, and T+18 suggest an event between T0 and T+9 that led to a local reduction of BL θ_e between the RMW and $r = 120$ km. Note that the sea surface temperature averaged within 160 km of the WRF storm center varied slightly across these times, with high correlation to the TC motion. The sea surface temperature fluctuated from 29.2°C at T0, to 29.1°C at T+9, and back to 29.2°C at T+18 (not shown)—this indicates that changes to the sea surface temperature are likely not the cause of the local reduction of θ_e. The most-straightforward explanation for the local decrease in $\langle \theta_e \rangle$ is that low-entropy air from the free atmosphere descended via convective downdrafts or mixed downward into the BL in the vicinity of reduced BL $\langle \theta_e \rangle$, similar to findings by Riemer et al. (2010) and Smith et al. (2017). However, the azimuth-mean kinematic fields do not provide clear evidence that air descended or mixed down into the kinematic BL. The likely avenue by which BL $\langle \theta_e \rangle$ was reduced in this case is more effectively illustrated from the asymmetric perspective, which is examined next.

c. *Asymmetric evolution*

Figure 6 shows low-level fields of storm-relative radial velocity u, vertical velocity w, and equivalent potential temperature θ_e at T0, which are averaged azimuthally within four environmental shear-relative quadrants. In the left column of Fig. 6, low-level inflow exhibited some asymmetry at T0, with deeper inflow in the DSR and DSL quadrants. Near-surface inflow in excess of 14 m s^{-1} was more radially broad in the USR and DSR quadrants, downstream of the storm motion and in agreement with prior studies (Shapiro 1983; Kepert 2001; Kepert and Wang 2001; Barnes and Dolling 2013), pointing to asymmetric frictional forcing associated with the superposition of the TC motion vector on the vortex wind field. Given that Irma's motion heading was nearly orthogonal and to the right of the shear vector, these asymmetries corroborate prior observational evidence suggesting that low-level inflow is asymmetrically amplified downshear and downstream of a translating TC (e.g., Barnes and Dolling 2013; Zhang et al. 2013). The low-level w-field showed slight asymmetries at T0 in the simulation, with broader ascent above the kinematic BL downshear, and a stronger core of inner-eyewall ascent DSL. Respectively, these asymmetries were likely driven by the deeper inflow downshear and stronger interior BL inflow DSR, as air from the DSR quadrant rotated into the DSL quadrant, converged, and ascended therefrom. The right column of Fig. 6 depicts Irma's θ_e structure at T0, with all quadrants having a high-θ_e core inward of the RMW and horizontal θ_e surfaces at outer radii that flare upward in the interior. There was some asymmetry present in θ_e outside the RMW, with generally higher θ_e to the right of shear.

By T0, the simulation's deep-layer shear had increased to about 19 kt from 15 kt 6 h prior, which continued until sometime between T+6 and T+12 as the vortex tilt increased at T+9. Figure 7 presents the same fields as Fig. 6, but for T+9. Downshear inflow became stronger through depth, in coincidence with the enhanced deep-layer shear in the preceding hours. The USL quadrant had a more complicated transverse circulation at T+9, including a radially confined near-surface inflow maximum at the RMW, outflow along the BL top at $r >$ 70 km, and a region of weak near-surface inflow between radii of 80 and 120 km. Along with the outer region of outflow near and above the BL top, the strong radial gradient of BL inflow between the RMW and $r = 100$ km in the USL quadrant suggests local divergence, and thus descent of air into the BL. Vertical velocity in the USL quadrant shown in Fig. 7 confirms that descent across the BL top was occurring in the radial band between 40 and 80 km. This feature is similar to the subsidence that typifies a TC moat region, but only appeared to occur USL near T+9. Instead, this may be more representative of a descending inflow jet, which was identified as a component of secondary eyewall formation and an eyewall replacement cycle in the observational study of Fischer et al. (2020). However, this simulation did not exhibit any evident secondary eyewall or eyewall replacement as observed. Plots of θ_e show that the

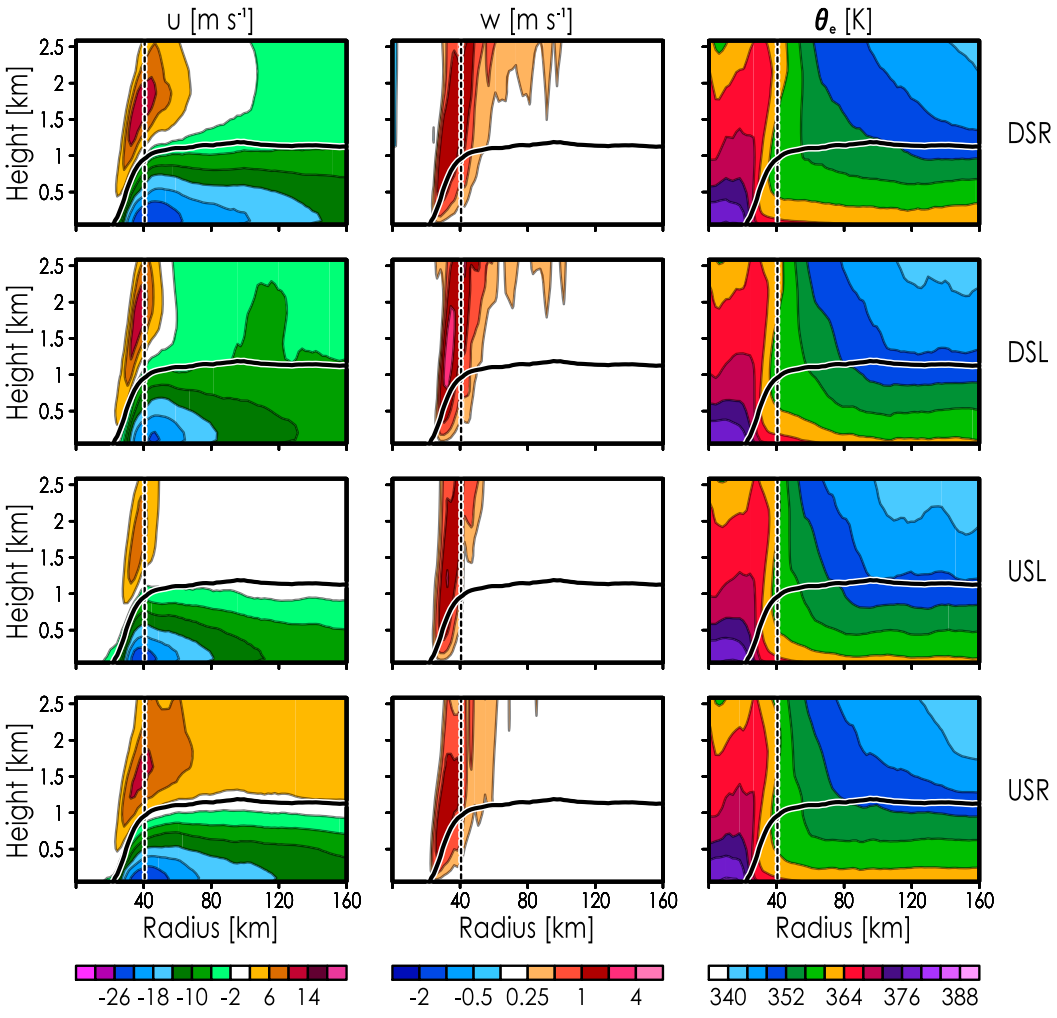

FIG. 6. Array of r–z cross sections depicting quadrant-mean (left) radial velocity u, (center) vertical velocity w, and (right) equivalent potential temperature θ_e during intensification at T0. Quadrants are determined using the environmental deep-layer shear and organized into rows (labels on the right margin). The dashed and thick, black lines in each plot are identical in definition to those in Fig. 5. All fields have been smoothed over 2 h. The scale used for w is geometric.

area of descent was also associated with a local minimum of BL θ_e, as low-entropy free atmospheric air was advected there from upwind of the descending inflow. The USL descent extends upward into the midtroposphere at T+9 (not shown), indicating that the terminus of strong inner-core inflow USL was collocated with deeper descent likely associated with shear-related convective asymmetry (DeHart et al. 2014).

In the USR quadrant at T+9, inflow was more radially homogeneous in the kinematic BL outside the RMW; this quadrant also contained the weakest peak inflow and a strong local maximum of outflow near the BL top at $r = 70$ km. The outflow overlying the USR kinematic BL was cyclonically shifted from asymmetrically strong tangential wind, shown at $z = 1.2$ km in the top row of Fig. 8. The azimuthal shift between radial and tangential wind dipoles seen in Fig. 8 could be explained by the advection of absolute angular momentum: BL inflow and convergence results in acceleration of v, culminating in supergradient winds and outward agradient forcing cyclonically downwind, and vice versa in regions of low-level outflow. This prospect is discussed further in section 5. Inward of $r = 120$ km, BL θ_e was greater USR than in the USL quadrant, in line with prior studies (e.g., Zhang et al. 2013) designating USR as a region for BL entropy recovery.

The lower levels of blended tail Doppler radar data available near T0 and T+9 can be examined to determine if the shear-relative inflow asymmetries are consistent between observations and the simulation; these data[2] are depicted in Fig. 9. The TC centers used for Fig. 9 is based loosely on the method used by Reasor and Eastin (2012): A subjective guess is made at the

[2] Blended radar data are from the NOAA/Hurricane Research Division's storm data archives (https://www.aoml.noaa.gov/hrd/Storm_pages).

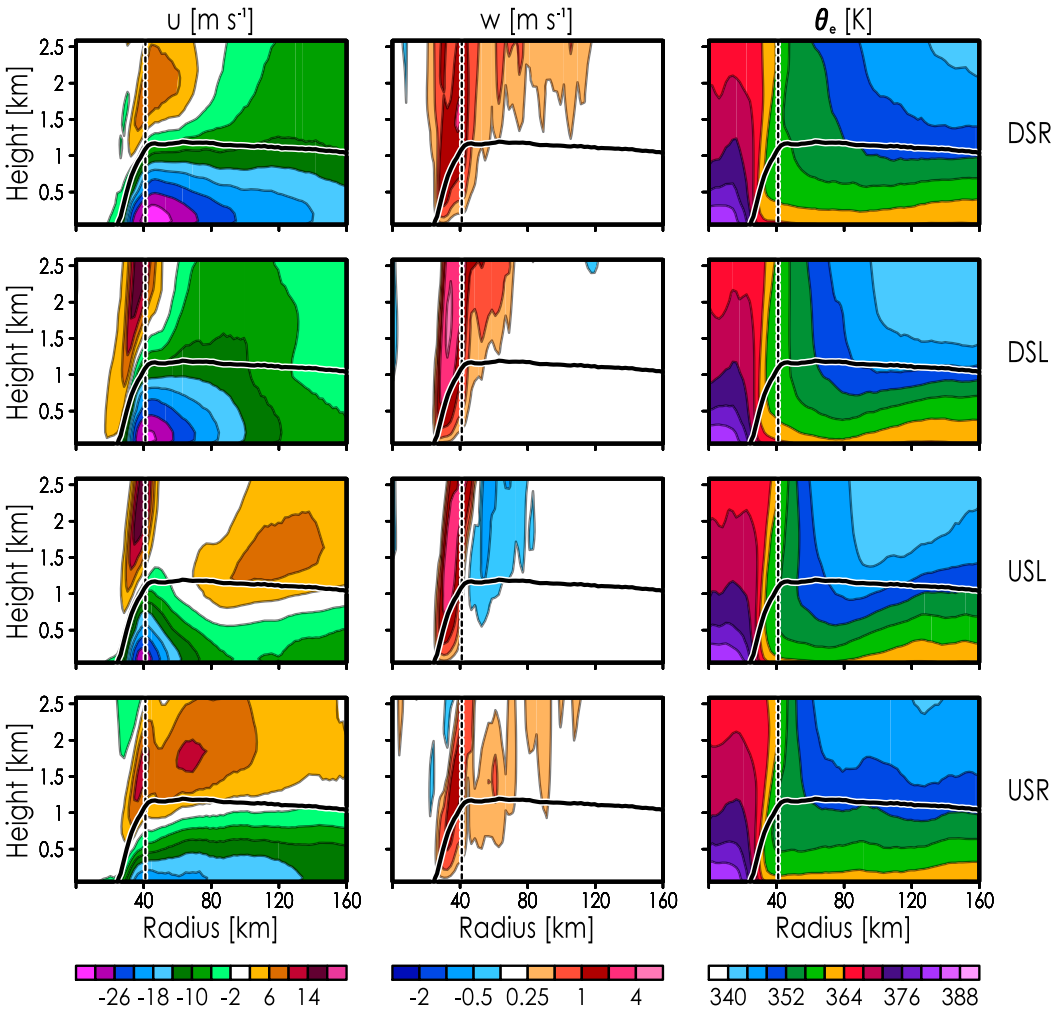

FIG. 7. As in Fig. 6, but during storm weakening at T+9.

TC center and the central radius of a 10-km radial band with complete azimuthal coverage that roughly captures the region where maximum azimuth-mean tangential winds are located. Then, the average of azimuth-mean tangential winds is calculated in the radial band based on TC centers every 0.01° within a 0.1° × 0.1° box centered on the first-guess TC center, and the center at which the maximum averaged azimuth-mean tangential wind is found is the next guess at the TC center. This process was repeated 2–3 times, after which the TC center converged to a point. In the top-left panel of Fig. 9, radial inflow at z = 1.5 km from ~T−2 to T+1 was oriented downshear and left of shear using the SHIPS deep-layer shear parameter, and generally in the entire downshear sector when using the local 2–9-km shear calculated by Fischer et al. (2020). Outflow and weak inflow were observed downstream of Irma's motion at z = 1.5 km, which may be too elevated for the frictional inflow asymmetries associated with storm motion to manifest (Shapiro 1983).

In both the simulation and observations, deeper low-level inflow was largely found downshear and on the south side of Irma near T0. Note that the observed shear metrics both had an eastward component, while the simulation's deep-layer shear metric had almost no zonal component at T0 (Fig. 4). In the bottom-left panel of Fig. 9 showing observed u from ~T+10 to T+13, the inflow depth asymmetry observed is similar when considering asymmetry relative to the local shear of ~11.8 kt, but not the SHIPS deep-layer shear, which was 1.5 kt at T+12. It is cautioned that the observed shear directions for this period are also quite different from the northerly shear in the simulation at T+9, so asymmetries associated with the shear in the simulation—at least from an Earth-relative perspective—may be inconsistent with Irma in reality. In the tangential wind fields, relatively strong v can be found on the north side of Irma, cyclonically shifted from the inflow to the east and southeast of Irma. This reflects a similar shift between u and v fields along azimuth to what was seen in the simulation (Fig. 8), as does the observed outflow located west to northwest of Irma (upshear or USL of the local shear), downwind of the stronger inner-core tangential winds on Irma's north side.

After T+9 and into T+18, deep-layer shear slackened to 15 kt and became more northwesterly, while Irma's motion

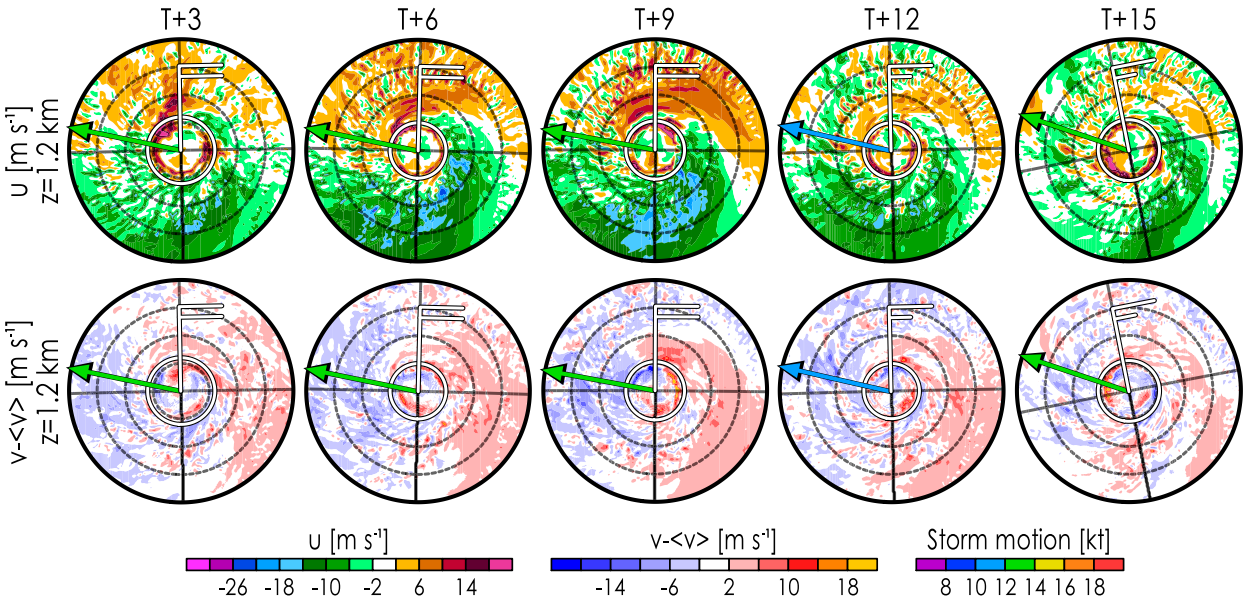

FIG. 8. Array of plan-view plots of (top) u and (bottom) azimuthal anomaly of tangential wind $v - \langle v \rangle$ at $z \approx 1.2$ km every 3 h from T+3 to T+15 (arranged in columns). Radius is plotted every 40 km using black concentric circle contours out to 160 km. The RMW is indicated in each plot with a thick white circle contour. Colored vectors and wind barbs represent storm motion and shear, as in Fig. 4.

became more counteraligned to the shear, oriented firmly within the USR quadrant. Figure 10 breaks down low-level u, w, and θ_e at T+18, as Irma resumed intensification. Near-surface inflow was asymmetrically strong upshear near the RMW, possibly associated with storm motion and shear turning, such that motion was directed more upshear. Above the kinematic BL, u showed less asymmetry than at T+9, with weak low-level inflow at most radii outside the RMW in the DSL quadrant, and strong inner-core outflow in the USR and DSR quadrants. Radial and vertical velocities upshear at T+18 suggested a secondary region of BL convergence and low-level ascent in the radial band between 80 and 120 km, which was also reflected in an upward bend of θ_e contours USL at ~120-km radius, and also USR at ~90-km radius. The secondary region of convergence and ascent appeared transiently for a few hours after T+18. Figure 10 shows that no substantial descent of low-θ_e air into the BL occurred in the radial band between 40 and 80 km at T+18, suggesting that the descent seen in the USL quadrant at T+9 may have been isolated to Irma's weakening phase. Next, the potential development of Irma's descending inflow is examined near T+9, including explanations for the descent that appeared in the USL quadrant.

4. Hurricane Irma's descending inflow

To understand further the thermal structure of Irma near T+9, Fig. 11 shows planview snapshots of θ_e at $z \approx 1.2$ km and $z \approx 210$ m. Outside the RMW, the u-field had a prominent dipole near the BL top from T+3 to T+9 (Fig. 8), with inflow downshear and outflow upshear. Low-θ_e air was located to the left of shear at the same height, wrapping cyclonically inward toward the RMW along the leading edge of inflow. A similar pattern appears within the inner-core at $z \approx 210$ m, with low-θ_e air spiraling inward from DSL at $r \approx 80$ km toward the RMW upshear (mainly USL) at T+9. Provided that descent was clearly occurring USL across the BL top near T+9 as shown in Fig. 7, the presence of low-θ_e inner-core air in that quadrant within the BL is reasonable. At least from these snapshots of u and θ_e, it appears that the low-θ_e air swirled inward along the amplified inflow DSL near the BL top, which then descended well into the BL in the USL quadrant. After T+9 when deep-layer shear drops to ~15 kt and vortex tilt is reduced, the dipole of u near the BL top becomes less pronounced as downshear inflow and upshear outflow weaken. To the left of shear, inner-core θ_e at the top and within the BL appears to recover after T+9.

The development of low-entropy air in the USL near-surface inflow near T+9 would presumably be ingested by eyewall convection downwind, affecting low-level buoyancy and thus the vertical acceleration of air parcels, provided that entropy is not completely recovered along the way by surface turbulent fluxes. The downshear tilt may also affect vertical ascent, should these low-entropy BL parcels from USL translate cyclonically into the downshear sector (Rios-Berrios et al. 2018; Ryglicki et al. 2018). The low-level thermal buoyancy b_T (Eastin et al. 2005; Rios-Berrios et al. 2018; Ryglicki et al. 2018) is defined as

$$b_T \equiv g\frac{\theta'_\rho}{\overline{\theta_\rho}}, \quad \text{with} \tag{2}$$

$$\theta_\rho \equiv \theta\left(\frac{1 + r_v/\varepsilon}{1 + r_v + r_{\text{total}}}\right), \tag{3}$$

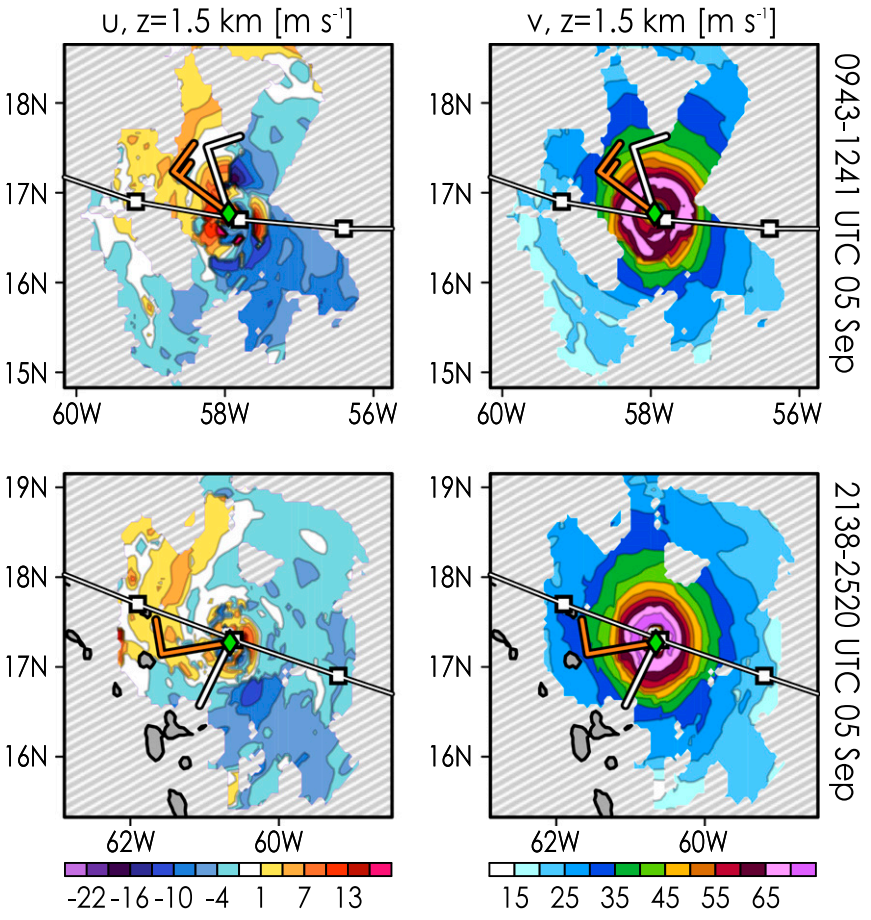

FIG. 9. Storm-relative (left) radial and (right) tangential velocities at $z = 1.5$ km as observed from tail Doppler radar on board NOAA WP-3D missions (top) 20170905H1 and (bottom) 20170905H2. The time period covering when swath data were collected is listed along the right side of each row, with times greater than 2400 signifying that the observations continued into the next day. The white line with square points represents the best-track path, with the squares denoting 6-hourly data. White wind barbs represent the 6-hourly SHIPS deep-layer shear data recorded during the observational periods. Orange wind barbs are the 2–9-km local shear determined for the mission by Fischer et al. (2020). Storm centers used to calculate the winds are indicated with green diamonds. Solid gray areas represent land, and dashed gray areas represent regions without data.

where $g = 9.81\,\mathrm{m\,s^{-2}}$ is the gravitational acceleration, θ_ρ is the density potential temperature, $\overline{\theta_\rho}$ is the base state of θ_ρ, θ'_ρ is the perturbation from the base-state density potential temperature, r_v is the mixing ratio of water vapor, $\varepsilon = 0.622$ is the ratio of gas constants for dry air and water vapor, and θ is the potential temperature. At each 2 km in radius at $r =$ 11 km and outward, the base-state density potential temperature is computed as the azimuth-mean θ_ρ averaged over a 20-km radial band and smoothed using a 2-h moving average in time. The resulting b_T at T0, T+9, and T+18 at $z = 720$ m is shown in Fig. 12. At T+9, low b_T values between −7 and $-3\,\mathrm{cm\,s^{-2}}$ are seen between 30- and 80-km radii in the USL quadrant, which extend cyclonically along and inward of the RMW in the USR quadrant. Note that these b_T values at T+9 in the upshear inner core are lower than those seen at T0 and T+18, supporting the suggestion that low-entropy air descending into the BL in the USL quadrant affected local low-level buoyancy. Findings were similar in calculations of b_T at $z \approx 210$ m and $z \approx 1.2$ km (not shown).

Given the link between inner-core convection and intensity (e.g., Hendricks et al. 2004; Montgomery et al. 2006; Nolan et al. 2007; Riemer et al. 2010; Hazelton et al. 2017a), it is suspected that the potential import of low-entropy air into eyewall convection upshear could contribute, at least in part, to Irma's intensity decline near T+9. This prospect is investigated qualitatively in Fig. 13, which shows cross sections of w at multiple times through most of the troposphere in the USR quadrant. Between T−3 and T+3, ascent in the midtroposphere appears to amplify in radial width and strength, although a neighboring cell of descent persisted along the inner edge of ascent, as well. By T+6, when environmental

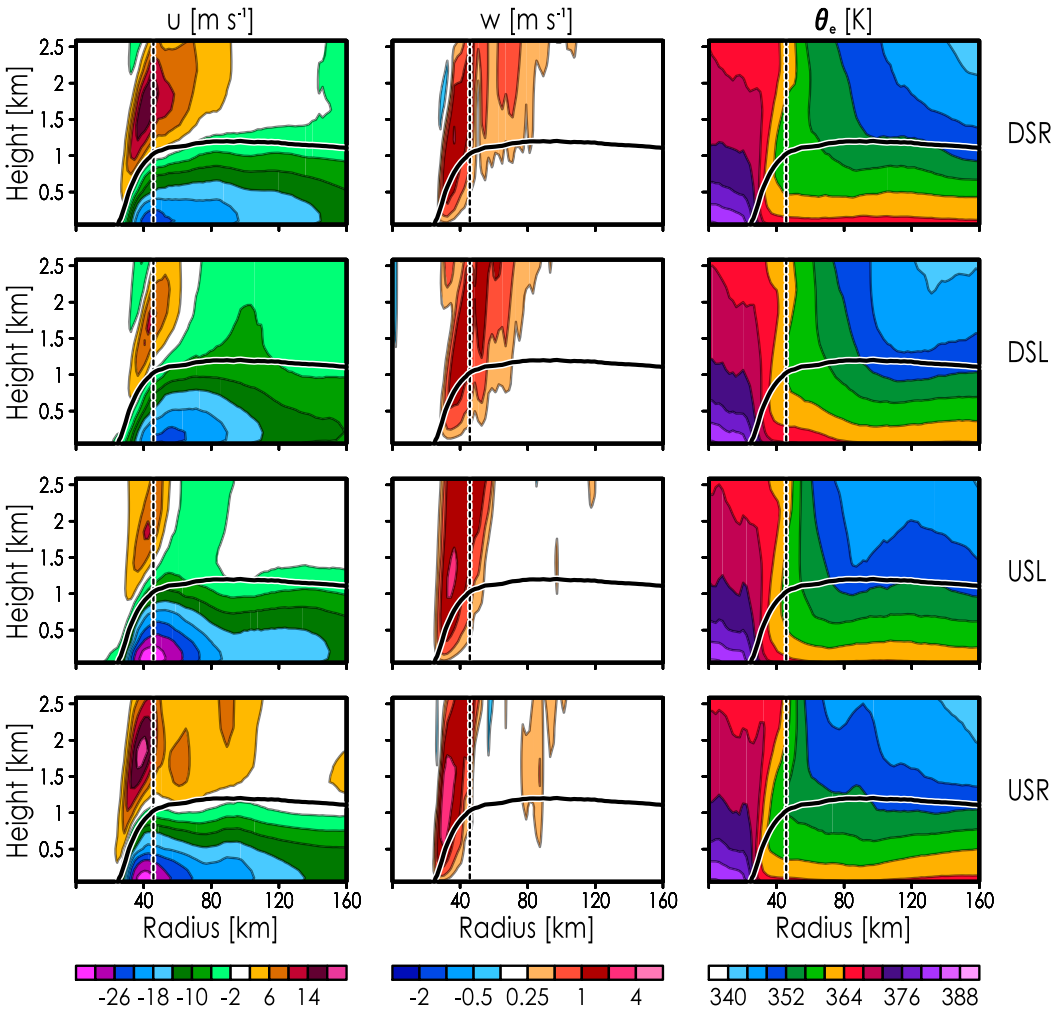

FIG. 10. As in Figs. 6 and 7, but during intensification at T+18.

shear reached its maximum magnitude, midtropospheric ascent became more narrow. This narrow midtropospheric ascent continued into T+9 (during weakening) and T+12 (less than an hour after weakening), while weak and shallow ascent formed in the low- to midtroposphere at multiple radii outside the eyewall. By T+15 and T+18, USR eyewall ascent had amplified throughout most of the troposphere. Figure 14, which shows the time evolution of w averaged between 4 and 12 km height in the USR quadrant, also suggests that mid- to upper-level vertical motion was affected as shear increased prior to T+9. As Irma transitioned from an intensification period into the weakening period at T+9, the inner edge of mid and upper-level ascent migrated radially outward as the width of ascent decreased, indicating an increase in the slope of USR eyewall convection. The ascent in Fig. 14 shifted inward around T+10 near the end of the weakening period, and the width and amplitude of ascent increased after Irma resumed intensification near T+15.

Note that even if the formation of low-θ_e air in the USL BL managed to weaken mid- to upper-tropospheric ascent in the eyewall downwind, it does not necessarily mean that the low-θ_e air caused Irma's weakening near T+9. It is possible that the formation of low-θ_e air was a consequence of dynamical changes related to increased shear (Jones 1995), such as increased vortex tilting at T+9 shown earlier in Fig. 3, that are actually responsible for Irma's weakening. However, the consequential low-θ_e air in that case could contribute to intensity tendency negatively until the tilt adjusts such that the midlevel vortex is moved cyclonically into USL (Rios-Berrios et al. 2018). To get a better sense of the timing of the changes in shear relative to changes in the BL and intensity, and thus perhaps an idea of causality, Fig. 15 shows time series of deep-layer shear, radial velocity asymmetry at $z \approx 1.2$ km between $r = 40$ km and $r = 80$ km (represented by a kinetic energy term $\mathrm{KE_{ua}}$), USL vertical mass flux at the same height and radial band F_w, and intensification rate. Here, $\mathrm{KE_{ua}}$ is defined as the kinetic energy associated with the departure of u from its azimuthal mean, averaged over the area of concern:

$$\mathrm{KE_{ua}} = \frac{1}{A}\iint_R \frac{(u - \langle u \rangle)^2}{2} dA, \qquad (4)$$

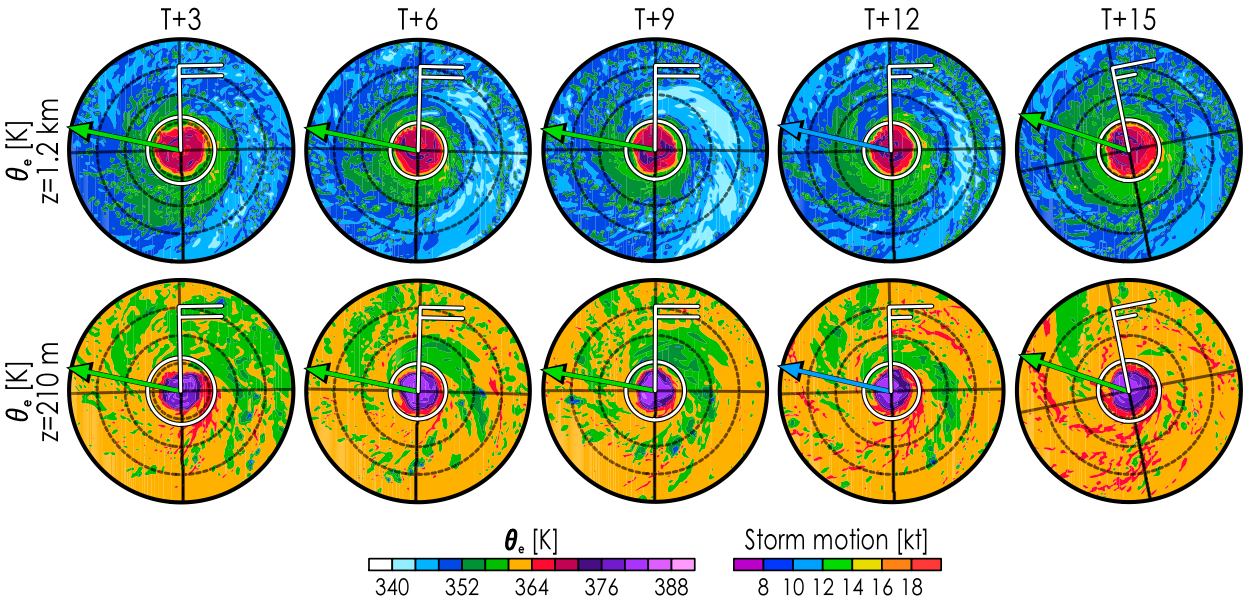

FIG. 11. As in Fig. 8, but showing θ_e at (top) $z \approx 1.2$ km and (bottom) $z \approx 210$ m.

where R in this case is the ring between $r = 40$ km and $r = 80$ km and A is its area. The USL vertical mass flux is calculated as

$$F_w = \frac{4}{A}\iint_S \rho w \, dA, \tag{5}$$

where S is the sector of the ring R in the USL quadrant, w is the vertical motion, and ρ is the air density. For this analysis of KE_{ua} and F_w, all fields are at $z \approx 1.2$ km.

The local deep-layer shear in Fig. 15 is similarly defined to the environmental deep-layer shear, except winds at 850 and 200 hPa are averaged within a 200-km radius (as opposed to a 200–800-km ring). A key advantage of using the local shear in this case is that it can be computed on the high-frequency (15 min) output of the innermost domain, providing much greater temporal resolution. Both the environmental and local shear increased starting at T−6, both becoming ~19 kt by T0. The local shear increased from ~20 kt to 24 kt leading up to T+3, while the environmental shear increased slightly between T0 and T+6 to about 21 kt. Prior to the maximization of local shear near T+3, KE_{ua} fluctuated between ~5 and 10 $m^2 s^{-2}$ with a period of about 4 h. Between T+3 and T+8, KE_{ua} increased toward a maximum of 25 $m^2 s^{-2}$, at which point u was most asymmetric near the BL top. Between T+4 and T+8 (nearly the same time as the increase of KE_{ua}), F_w became negative as Irma stopped intensifying and began to weaken, with $F_w \approx -30 \times 10^{-2}$ kg $m^{-2} s^{-1}$ by T+8. As local and environmental shear decreased after T+8, KE_{ua} also decreased while F_w increased and became positive once again. These

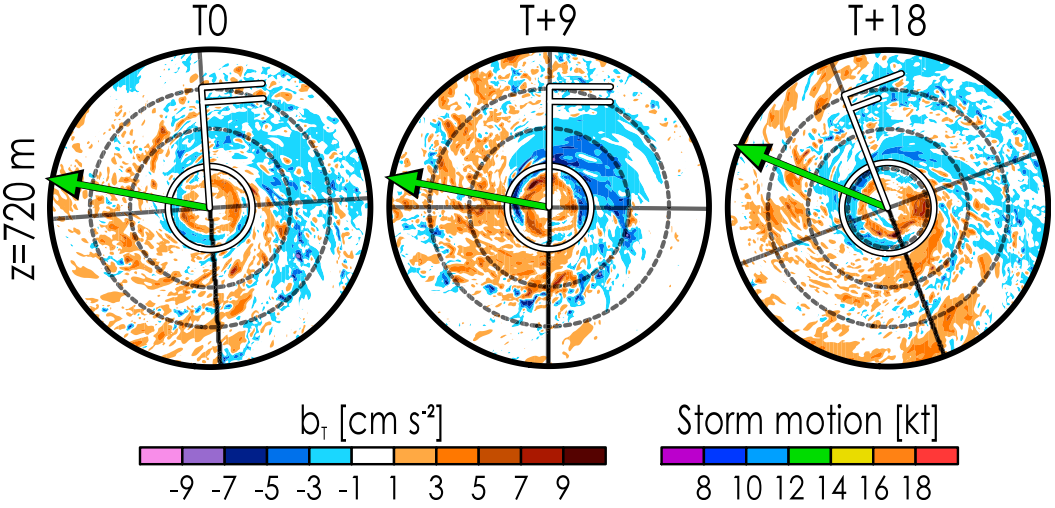

FIG. 12. As in Fig. 8, but showing the thermal buoyancy b_T at $z = 720$ m, every 9 h from T0 to T+18.

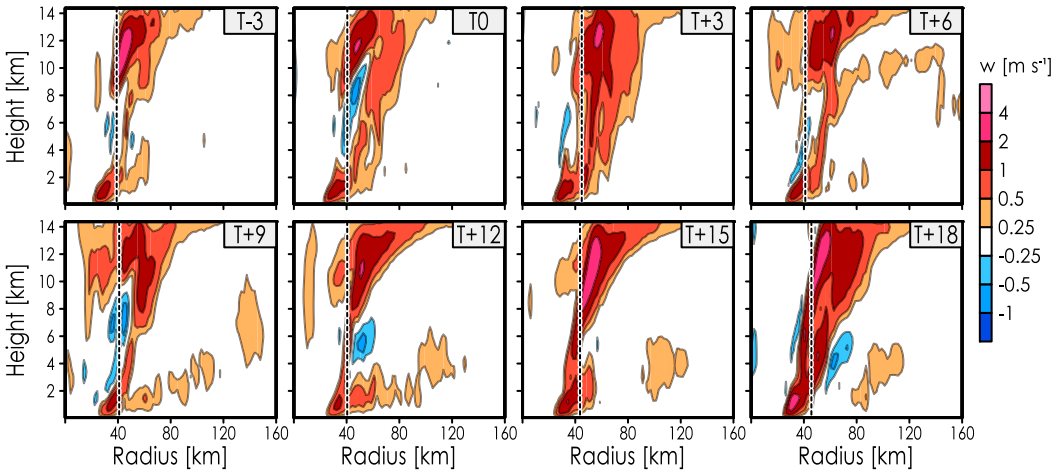

FIG. 13. Radius–height cross sections of vertical motion w in the lowest ~14 km of the USR quadrant, every 3 h between T−3 and T+18. The RMW is marked in each plot with a dashed line. Fields have been smoothed over 2 h.

trends continued into Irma's next intensification period that began near T+15.

Between T0 and T+18, it is evident and shown explicitly in Fig. 16 that the intensification rate was negatively correlated with the radial velocity asymmetry, and also positively correlated with the USL vertical mass flux just outside the RMW. The Pearson correlation coefficients were $\chi = -0.885$ for intensity tendency versus KE_{ua} and $\chi = 0.916$ for intensity tendency versus F_w in the USL quadrant. Pearson correlations between intensity tendency and F_w calculated in other quadrants were weaker, with $\chi = 0.517$ using DSL, $\chi = 0.032$ using DSR, and $\chi = 0.834$ using USR. The time-average of F_w across Irma's weakening period differed from those across Irma's intensifying periods encapsulating T0 and T+18 to a statistically significant degree (to 99.9% confidence using an unequal-size, two-sample t test). This result suggests that the downward flux of air in the USL quadrant as previously described is unique to the highlighted weakening phase about T+9, which supports the suspicion as to the reason for Irma's weakening.

With regard to causality (e.g., what caused low-θ_e air to descend into the USL inner-core BL, or what caused Irma's weakening), the local shear increased rapidly starting at T+2, about 1 h before a sharp increase in KE_{ua} and a decrease in F_w. The intensification rate also began to increase just after T+9, about an hour after the local shear and KE_{ua} began to rapidly decrease and F_w began to increase. However, it is difficult to discern whether an hour of separation between these events is sufficient to indicate causality, as these fields are subject to a degree of randomness. Note that an assessment of vertical motion aloft revealed that downdrafts originating in the mid- to upper troposphere occurred intermittently in the inner-core of the USL quadrant between T0 and T+9 (not shown), although these downdrafts tended to terminate above $z = 2$ km and did not appear in an areal average of w between $r = 40$ km and $r = 80$ km. Also note that the time series of vertical mass flux and u asymmetry indicated no obvious trends prior to T+3, despite a substantial increase in deep-layer shear. Restraint to discern causality from these data vis-à-vis deep-layer shear, BL asymmetry, and intensification rate is taken here, but it is clear that they are correlated—at least in this case between T0 and T+18.

5. Formation of upshear-left outflow and descent near the BL top

If one assumes that the deep-layer shear and/or vortex tilt is physically linked to and perhaps responsible for the BL's

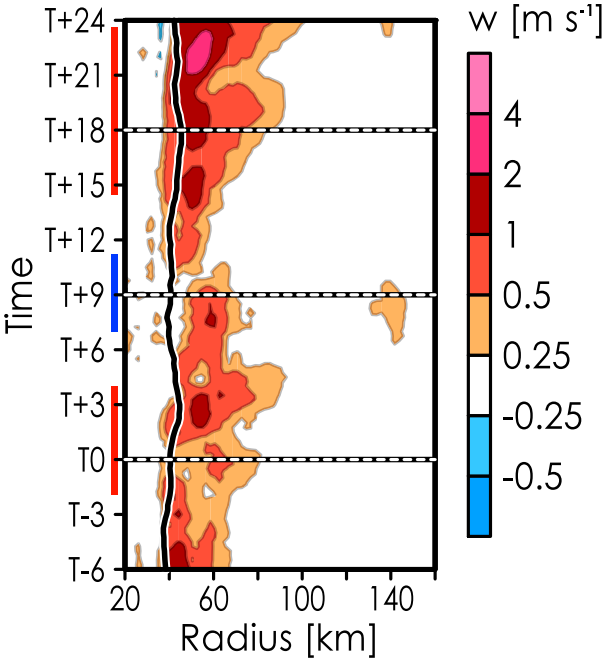

FIG. 14. Radius–time Hovmöllers of w, averaged between $z = 4$ km and $z = 12$ km in the USR quadrant. Red and blue bars along the time axis indicate periods of intensification and weakening, respectively. The thick, solid black line represents the RMW, and dotted horizontal lines mark T0, T+9, and T+18. Fields have been smoothed over 2 h.

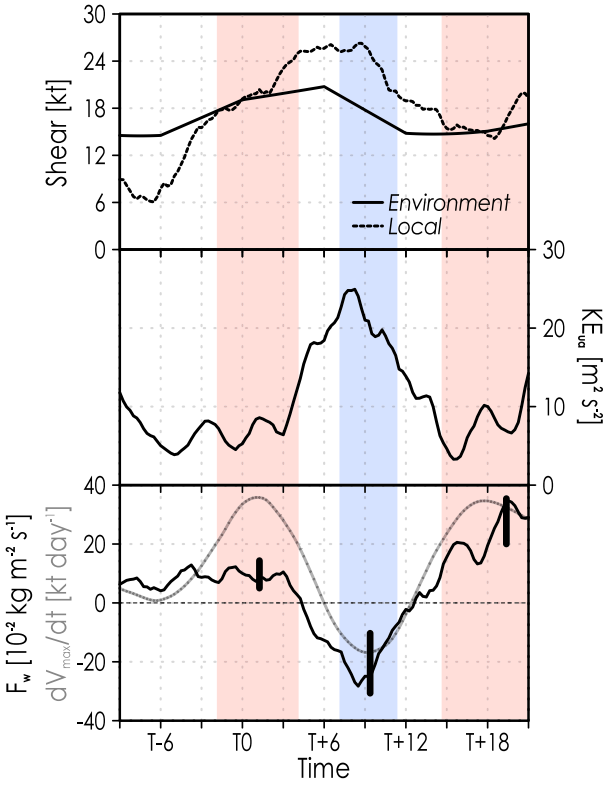

FIG. 15. Time series of (top) deep-layer shear, (middle) radial velocity asymmetry at $z \approx 1.2$ km (KE_{ua}), and (bottom) vertical mass flux at $z \approx 1.2$ km in the USL quadrant (F_w; thin black line). Intensity tendency is also plotted in gray in the bottom panel. Red and blue shading are used to delineate periods of intensification and weakening, respectively. In the top panel, the environmental shear is plotted (solid line) along with local shear (dotted line), which is calculated over the same depth using winds within 200 km of Irma's center on the innermost domain. In each intensification and weakening period in the bottom panel, a thick vertical line denotes the 99.9% confidence interval for the mean F_w across the period.

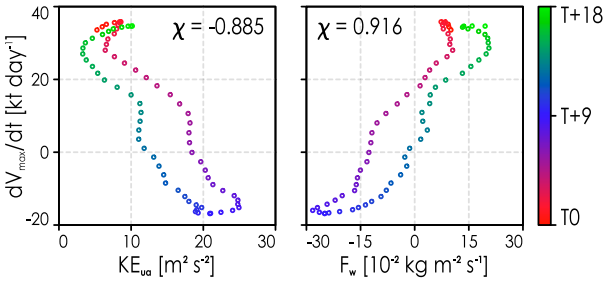

FIG. 16. Scatterplots of intensity tendency as a function of (left) radial velocity asymmetry at $z \approx 1.2$ km and (right) vertical mass flux at $z \approx 1.2$ km in the USL quadrant. Data points are taken from T0 to T+18 and are shaded by time. Each scatterplot contains its Pearson correlation coefficient χ.

azimuthal structure in this case, how *could* it drive changes in the azimuthal structure of the BL? More specifically, how could the shear be linked to the appearance of descent across the BL top in the USL quadrant? If the shear effectively acts to increase both the depth and strength of low-level inflow downshear, then momentum and entropy tendencies from radial advection would likely be affected downshear. For example, changes in upper tropospheric outflow associated with shear could impart a change in upper-level divergence, thereby affecting the secondary circulation and advection along its circuit. (An exception to the presumed effects on radial advection would be if the radial gradients of advected properties weakened to offset the effect of increased inflow). Via this logic, M advection along the inflow down the pressure gradient would be amplified downshear, leading to an increased local spinup tendency. That spinup tendency would factor into Coriolis and centrifugal forces associated with gradient-wind balance, leading v to become more locally supergradient or less subgradient. Spinup tendency from M advection is offset in the BL by friction, but note again that the downshear sector's inflow is also *deeper*. The effect of friction is reduced with increasing altitude, so frictional spindown may not entirely counter the spinup from M advection through the depth of a deep low-level inflow layer. One may then expect v along the leading edge of enhanced inflow to become anomalously strong in the azimuthal sense and more supergradient, especially near and above the kinematic BL top—to clarify, the kinematic BL is defined in this work using the azimuth-mean inflow. Figure 8 reveals these features in this simulation of Irma most evidently at T+9.

The horizontal momentum equations can be used to investigate how tangential and radial flows evolve in more detail:

$$\frac{\partial v}{\partial t} = \mathrm{GCF} - \frac{v}{r}\frac{\partial v}{\partial \lambda} - w\frac{\partial v}{\partial z} - \frac{1}{\rho r}\frac{\partial p}{\partial \lambda} + D_v \quad \text{and} \tag{6}$$

$$\frac{\partial u}{\partial t} = \mathrm{AGF} - u\frac{\partial u}{\partial r} - \frac{v}{r}\frac{\partial u}{\partial \lambda} - w\frac{\partial u}{\partial z} + D_u, \tag{7}$$

where GCF represents the generalized Coriolis force (Smith et al. 2009)—the sum of the azimuthal Coriolis force, the radial flux of angular velocity, and also the radial advection of tangential momentum (included in Gu et al. 2016):

$$\mathrm{GCF} \equiv -fu - \frac{uv}{r} - u\frac{\partial v}{\partial r}, \tag{8}$$

and AGF represents the agradient force—the sum of the radial Coriolis, centrifugal, and radial pressure gradient forces:

$$\mathrm{AGF} \equiv fv + \frac{v^2}{r} - \frac{1}{\rho}\frac{\partial p}{\partial r}. \tag{9}$$

Also, $-(\rho r)^{-1}\partial p/\partial \lambda$, which represents the azimuthal pressure gradient force, is negligible for this analysis. The D_u and D_v are residual terms.

Radius–time Hovmöllers of various terms composing the horizontal momentum budget in the DSL quadrant at $z \approx 1.2$ km are shown in Fig. 17. As shear and vortex tilt increased between T0 and T+9, inflow generally strengthened outside the RMW in the DSL quadrant (i.e., $\partial u/\partial t < 0$). Over the same period, $\partial v/\partial t$ was often nonnegative near and outside the RMW, indicating local spinup. Agradient forcing increased

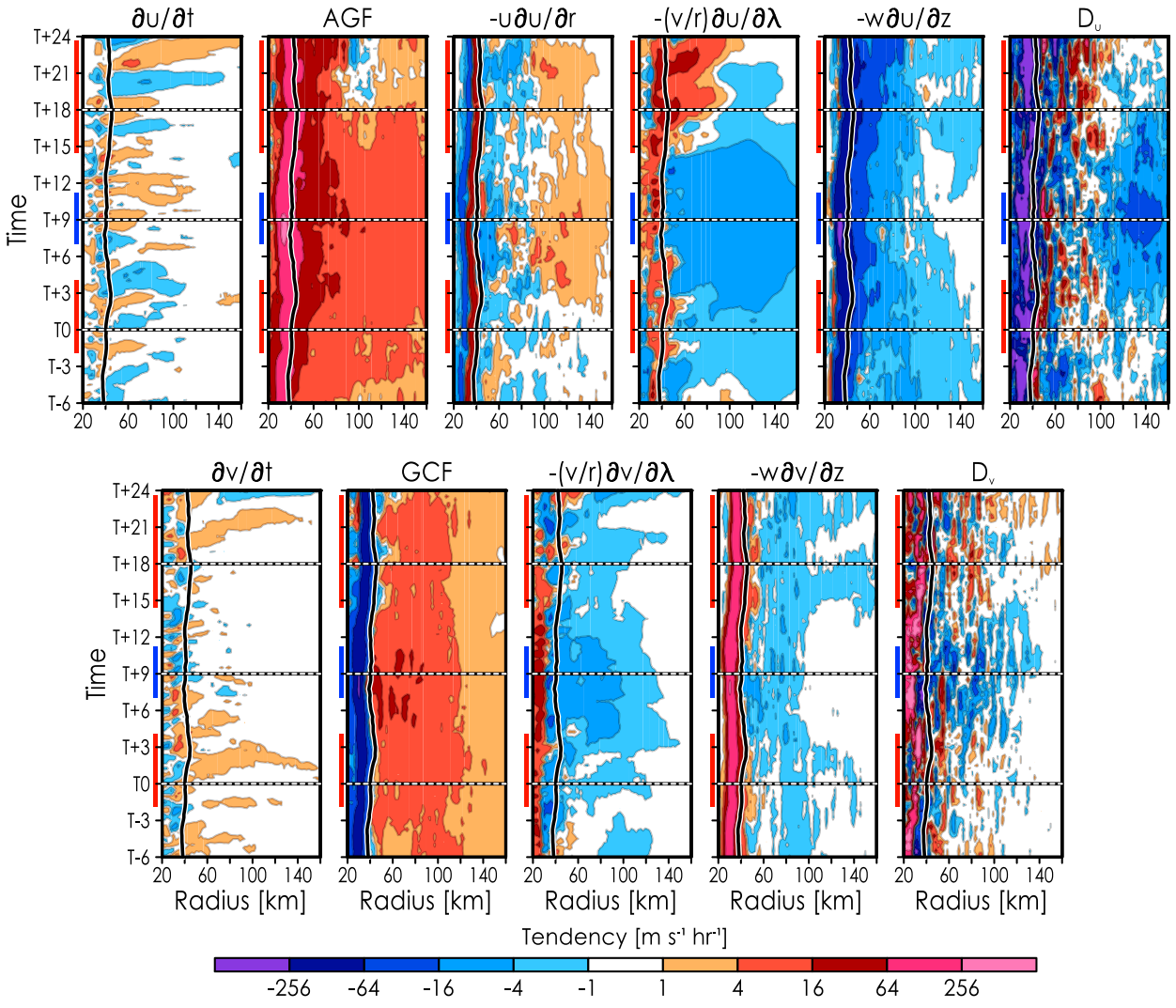

FIG. 17. Radius–time Hovmöllers of tendency terms ($m\,s^{-1}\,h^{-1}$) in (top) the radial momentum budget and (bottom) tangential momentum budget from Eqs. (6) and (7), taken at $z \approx 1.2$ km in the DSL quadrant. Red and blue bars along the time axis indicate periods of intensification and weakening, respectively. The thick, solid black line represents the RMW, and dotted horizontal lines mark T0, T+9, and T+18. All shown fields have been smoothed over 2 h. Tendency fields share the appropriately labeled color scale, which is geometric.

between the RMW and $r = 100$ km as v increased leading up to T+9. The positive $\partial v/\partial t$ is largely attributable to the GCF term—more specificially, the radial flux of angular velocity term $-uv/r$ included in the GCF. As local inflow and tangential wind increased between T0 and T+9, $-uv/r$ increased in kind, which accounts for most of the increase in GCF between the RMW and $r = 80$ km over that period. After T+9 and leading up to T+18, $\partial u/\partial t$ was often positive, indicating weakening inflow as the shear decreased. The change in u came with a decrease in AGF, as local v became less supergradient presumably due to a reduced radial influx of M. The radial advection of M is

$$-u\frac{\partial M}{\partial r} = r\left(-fu - \frac{uv}{r} - u\frac{\partial v}{\partial r}\right) = r \times \mathrm{GCF}, \qquad (10)$$

which is shown in a Hovmöller for the DSL quadrant at $z \approx 1.2$ km in the left panel of Fig. 18. The radial influx of M between the RMW and $r = 100$ km reached its peak near T+9, after which it began to decrease alongside a decrease in AGF.

As the flow evolved over time in the DSL quadrant, so too did the flow evolve downwind as air rotated cyclonically about the TC center into the USL quadrant. Similar to Fig. 17, Fig. 19 shows radius–time Hovmöllers of momentum budget terms in the USL quadrant near the BL top. A couple of hours prior to T0, u increased and became nearly zero outside of the RMW (not shown). Radial velocity continued to increase intermittently between T0 and T+9, with distinct periods of outward acceleration between the RMW and $r = 160$ km. A region of outflow developed at $r >$ 60 km just after T+3 (seen in Fig. 11 at T+6 and T+9), after

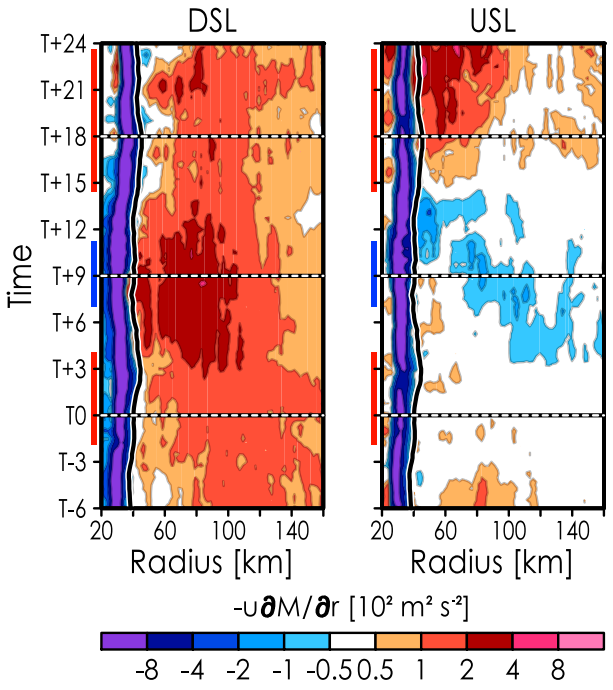

FIG. 18. Radius–time Hovmöllers of radial advection of absolute angular momentum $-u\partial M/\partial r$ ($10^2 \times m^2 s^{-2}$) in the (left) DSL and (right) USL quadrants at $z \approx 1.2$ km. Red and blue bars along the time axis indicate periods of intensification and weakening, respectively. The thick, solid black line represents the RMW, and dotted horizontal lines mark T0, T+9, and T+18. The fields have been smoothed over 2 h.

which Irma ceased intensification. Tangential momentum increased outside the RMW prior to the weakening phase, with a similar imprint of $\partial v/\partial t > 0$ between T0 and T+7 as that in the DSL quadrant. However, the time at which the aforementioned imprint appears in the USL quadrant is about an hour after its appearance in the DSL quadrant, suggesting that this positive tendency in v propagated from the DSL quadrant into the USL quadrant. In coincidence with these developments, AGF in the USL quadrant increased leading up to T+9 and was often stronger than the AGF in all other quadrants between the RMW and $r \approx 100$ km. In the examinations of the residual terms D_u and D_v, the terms are often negative and tend to oppose sums of the nonresidual terms in the momentum budgets. In other words, the effects of turbulent eddies and mixing are nonnegligible as evidenced by their similar magnitudes in the budget equation, and largely offset the nonresidual terms. Outside the RMW, the vertical mixing and diffusion, which are included in these terms, should distribute relatively low momentum (i.e., weaker v and more negative u) from the kinematic BL below $z = 1.2$ km into the plane of analysis. There are some exceptions, such as just inward of the RMW in D_v, which is likely due to vertical diffusive and flux terms associated with the presence and maintenance of the BL tangential wind jet (Kepert and Wang 2001; Williams 2015).

The increase of AGF in the USL quadrant occurred despite a nonnegative u-field at $r > 60$ km, which suggests nonpositive radial advection of M and implies local spindown. Indeed, the USL Hovmöller of $-u\partial M/\partial r$ in Fig. 18 illustrates that radial advection of M was often nearly zero or negative prior to T+15. This is noteworthy because positive radial advection of M is often referenced alongside vertical advection to explain the spinup of v and the presence of supergradient flow near the BL top, as in the axisymmetric framework posed by Smith et al. (2009).

How did v and the AGF increase in the USL quadrant leading up to T+9 if there was no substantial inward transport of high-M air? Fig. 19 indicates that increases in v and AGF leading up to T+9 in the USL quadrant were due to the *azimuthal advection* of tangential momentum, $-(v/r)\partial v/\partial\lambda$. (It is noted that the mass field did not substantially adjust to weaken the inward-directed radial pressure gradient force, which could otherwise possibly explain an increase in AGF.) The positive azimuthal advection of v implies that v became maximized and most supergradient to the left of shear leading up to T+9, which was advected into the USL quadrant by the cyclonic flow. Similarly, Gu et al. (2016) found that a weakening, mature TC under shear developed anomalously strong v left of shear, due to inward advection of M downshear and subsequent transport of enhanced tangential momentum downwind into the left-of-shear semicircle. In Irma's case, a response to alleviate the dynamical imbalance associated with supergradient v presumably emerged in the USL quadrant, wherein outflow at radii outside the RMW developed as the AGF increased and $\partial u/\partial t$ became positive. The development of outflow and radial divergence between the RMW and $r = 100$ km should be coincident with descent by mass continuity, which was shown in Fig. 15 and associated with Irma's weakening phase in section 4. This would be the case unless there was ample azimuthal convergence to offset the radial divergence, but between the RMW and about $r = 60$ km the azimuthal divergence field was about an order of magnitude weaker than the radial divergence, and the total horizontal divergence field was positive and dominated by radial divergence (not shown).

6. Summary and discussion

In this first part of a two-part analysis on asymmetric BL structure associated with TC intensity decline, results from a full-physics simulation of Hurricane Irma in 2017 are examined. Three periods in the simulation were in focus for this investigation, when Irma—a major hurricane throughout the time of analysis—underwent intensification, followed by a weakening phase, and then reintensification thereafter. Differences were noted between the simulation and observations in environmental shear and intensity change, indicating that structural features of the simulated storm should be viewed as a realistic forecast of Irma, rather than as a close representation of Hurricane Irma as observed.

Deep-layer shear and associated vortex tilt fluctuated across the analysis period, with strong shear developing during the first highlighted intensification period, and then more-moderate shear developing in the middle of the weakening

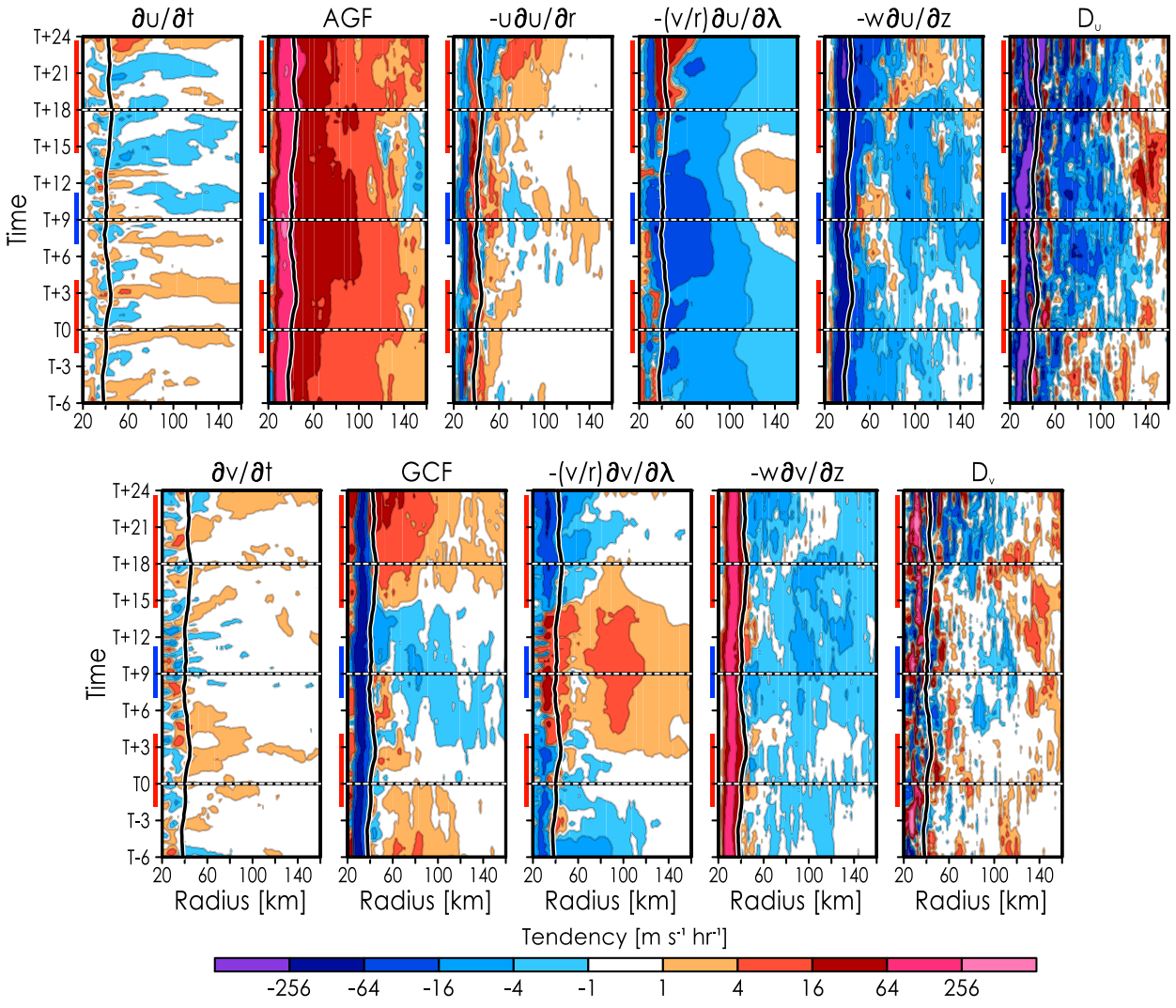

FIG. 19. As in Fig. 17, but showing tendency fields at $z \approx 1.2$ km in the USL quadrant.

phase that followed. Prior to the increase in deep shear, Hurricane Irma's inner-core exhibited a nearly axisymmetric low-level primary circulation, as well as a minimally asymmetric low-level secondary circulation and thermodynamic structure. Leading up to Irma's weakening phase, the low-level secondary circulation became more asymmetric in coincidence with increased shear and tilt. Specifically, stronger inflow developed downshear, which wrapped cyclonically inward from the DSR quadrant into the USL quadrant, while low-entropy air from the free atmosphere descended into the BL mainly in the USL inner-core (illustrated conceptually in Fig. 20). Note that recent findings by Wu et al. (2021) revealed a negative convective precipitation bias in the Morrison microphysics scheme employed here, implying that asymmetries associated with convective downdrafts, rainfall evaporation, and thus BL static stability (Kepert et al. 2016)—as seen in relation to the descent of low-entropy air USL—may be underrepresented. The low-entropy BL air in the USL quadrant was drawn into the eyewall region, which affected local buoyancy (Fig. 12) and likely the vertical acceleration of air in the eyewall, provided that surface turbulent fluxes of latent and sensible heat did not replenish such air parcels' entropy prior to arrival at the root of convection. In the sense that this would weaken deep convection in the eyewall, it is concluded that the import of low-entropy air into the inner-core BL that occurred in association with increased deep shear and vortex tilt is responsible, at least in part, for Irma's weakening near the end of 5 September in this simulation.

The vertical flux of air into the USL inner-core BL during Irma's weakening was persistently negative and significantly different from those calculated over Irma's intensification periods to 99.9% confidence. Along the inner-core BL top, the vertical flux of air in the USL quadrant was negatively correlated with the degree of asymmetry in radial velocity. Prior to Irma's weakening, the local shear was shown to increase rapidly about an hour before radial flow asymmetry increased and USL vertical mass flux decreased. During the weakening phase, Irma's intensity tendency began to increase

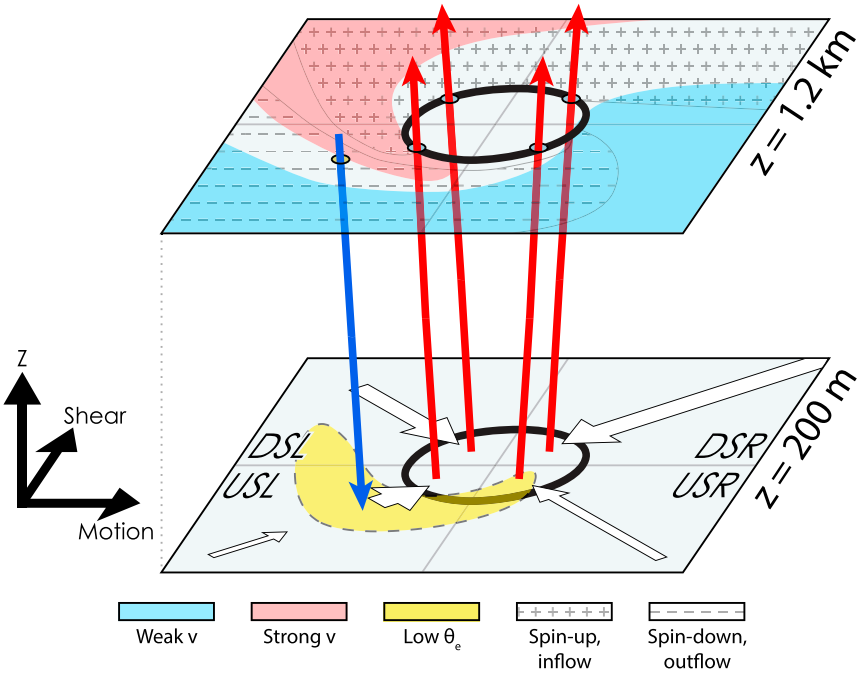

FIG. 20. Volumetric conceptual schematic of Hurricane Irma's simulated low-level, inner-core structure during weakening near T+9. Axes on the left side indicate vertical, TC motion, and deep-layer shear directions. Each horizontal plane is labeled by height on the right. Black circles at the center of each plane mark the RMW. White arrows represent quadrant-averaged BL radial flow, with thicker arrows for stronger flow. Red and blue arrows mark areas of quadrant-averaged ascent and descent, respectively. At $z = 200$ m, yellow shading resembles low-entropy air. At $z = 1.2$ km, areas of spinup (inflow) and spindown (outflow) are marked with pluses and minuses, respectively. Asymmetrically strong v is indicated in red shading, and asymmetrically weak v is indicated in blue shading.

about an hour after a decrease in local shear, a decrease in radial flow asymmetry, and an increase in USL vertical mass flux. While caution must be taken to draw conclusions as to what caused the BL asymmetries to develop, including those in the secondary circulation and θ_e that are potentially behind Irma's weakening, there is an evident link in this case between the deep-layer shear, BL asymmetry, and intensity tendency.

The localized descent in the USL BL during weakening was associated with an outward acceleration of u, which itself became positive (outflow) and was linked to an increase in BL divergence. The outward tendency in USL radial flow was associated with increased agradient forcing (i.e., v becoming more supergradient), as v became anomalously strong USL. The spinup of inner-core v in the USL quadrant, however, was not due to local radial advection of M, while the azimuthal advection of v was a primary contributor to the quadrant's positive v tendency. This is because v was maximized upwind of the USL quadrant in the azimuthal sense, which would be expected given the amplified radial inflow and consequent spinup from radial advection of M in the downshear sector. To wit, the shear (as well as the increased tilt) was associated with amplified inflow, positive radial advection of M, and subsequent spinup downshear; the resulting supergradient v was advected cyclonically into the USL quadrant, where strongly positive AGF led to a positive tendency in u, the development of outflow outside the RMW, and thus BL divergence and descent. By contrast, the upshear sector was associated with weaker low-level inflow and the presence of outflow above the BL; and v in the right-of-shear semicircle was weaker than left of shear, allowing Irma's intensity—a measure of azimuth-mean v in this study—to decrease despite an amplification of v in the USL quadrant. Similar patterns and associated changes in azimuth-mean v (i.e., intensity as defined here) were found in an analysis by Gu et al. (2016) of the evolution of an idealized TC's low-level tangential wind jet under shear.

In Part II to follow, the simulated BL structure of Hurricane Earl (2010) will be examined, which exhibited relatively pronounced asymmetries in comparison with Irma, formed a secondary eyewall, and underwent eyewall replacement. Therein, a discussion of how differences in shear and storm motion might account for the different structural evolutions of these two cases is provided. Among these differences between the two cases is the orientation of the shear relative to the TC motion, which will be highlighted as a possible explanation, at least in part, for the differences in simulated BL structures. Notably, Part II will outline how asymmetric low-level outflow in response to azimuthally local dynamical imbalances associated with

shear and TC motion could contribute to the radial expansion of the primary circulation, and to that end, provide an impetus for secondary eyewall formation.

Acknowledgments. The authors appreciate all of the helpful suggestions and critique that Drs. Xiaomin Chen and Jun Zhang provided that strengthened this work and its paper. The authors also thank three anonymous reviewers for their attentive and constructive comments and recommendations, which further improved and refined this work. This research was funded by the Ocean Observing and Monitoring Division of the National Oceanic and Atmospheric Administration's Climate Program Office (FundRef 100007298) via the Northern Gulf Institute under Grant NA16OAR4320199 and NOAA Awards NA17OAR4310153 and NA19OAR0220186 and by NASA Physical Oceanography's funding for the Ocean Vector Winds Science Team.

Data availability statement. All data and tools used in the current work are publicly available and accessible online, including WRF-ARW Model source code and documentation, initial and boundary conditions for the model, and GrADS data visualization software. Model output cannot be shared explicitly because of its large size, but it can be replicated using the method provided.

REFERENCES

Ahern, K., and L. Cowan, 2018: Minimizing common errors when projecting geospatial data onto a vortex-centered space. *Geophys. Res. Lett.*, **45**, 12 032–12 039, https://doi.org/10.1029/2018GL079953.

——, M. A. Bourassa, R. E. Hart, J. A. Zhang, and R. F. Rogers, 2019: Observed kinematic and thermodynamic structure in the hurricane boundary layer during intensity change. *Mon. Wea. Rev.*, **147**, 2765–2785, https://doi.org/10.1175/MWR-D-18-0380.1.

Alduchov, O. A., and R. E. Eskridge, 1996: Improved Magnus form approximation of saturation vapor pressure. *J. Appl. Meteor.*, **35**, 601–609, https://doi.org/10.1175/1520-0450(1996)035<0601:IMFAOS>2.0.CO;2.

Barnes, G. M., 2008: Atypical thermodynamic profiles in hurricanes. *Mon. Wea. Rev.*, **136**, 631–643, https://doi.org/10.1175/2007MWR2033.1.

——, and K. P. Dolling, 2013: The inflow to Tropical Cyclone Humberto (2001) as viewed with azimuth-height surfaces over three days. *Mon. Wea. Rev.*, **141**, 1324–1336, https://doi.org/10.1175/MWR-D-11-00348.1.

Black, M., J. Gamache, F. Marks, C. Samsury, and H. Willoughby, 2002: Eastern Pacific Hurricanes Jimena of 1991 and Olivia of 1994: The effect of vertical shear on structure and intensity. *Mon. Wea. Rev.*, **130**, 2291–2312, https://doi.org/10.1175/1520-0493(2002)130<2291:EPHJOA>2.0.CO;2.

Bolton, D., 1980: The computation of equivalent potential temperature. *Mon. Wea. Rev.*, **108**, 1046–1053, https://doi.org/10.1175/1520-0493(1980)108<1046:TCOEPT>2.0.CO;2.

Chavas, D. R., 2017: A simple derivation of tropical cyclone ventilation theory and its application to capped surface entropy fluxes. *J. Atmos. Sci.*, **74**, 2989–2996, https://doi.org/10.1175/JAS-D-17-0061.1.

Chen, S. S., J. A. Knaff, and F. D. J. Marks, 2006: Effects of vertical wind shear and storm motion on tropical cyclone rainfall asymmetries deduced from TRMM. *Mon. Wea. Rev.*, **134**, 3190–3208, https://doi.org/10.1175/MWR3245.1.

Chen, X., Y. Wang, J. Fang, and M. Xue, 2018a: A numerical study on rapid intensification of Typhoon Vicente (2012) in the South China Sea. Part II: Roles of inner-core processes. *J. Atmos. Sci.*, **75**, 235–255, https://doi.org/10.1175/JAS-D-17-0129.1.

——, M. Xue, and J. Fang, 2018b: Rapid intensification of Typhoon Mujigae (2015) under different sea surface temperatures: Structural changes leading to rapid intensification. *J. Atmos. Sci.*, **75**, 4313–4335, https://doi.org/10.1175/JAS-D-18-0017.1.

Corbosiero, K. L., and J. Molinari, 2002: The effects of vertical wind shear on the distribution of convection in tropical cyclones. *Mon. Wea. Rev.*, **130**, 2110–2123, https://doi.org/10.1175/1520-0493(2002)130<2110:TEOVWS>2.0.CO;2.

——, and ——, 2003: The relationship between storm motion, vertical wind shear, and convective asymmetries in tropical cyclones. *J. Atmos. Sci.*, **60**, 366–376, https://doi.org/10.1175/1520-0469(2003)060<0366:TRBSMV>2.0.CO;2.

DeHart, J. C., R. A. Houze Jr., and R. F. Rogers, 2014: Quadrant distribution of tropical cyclone inner-core kinematics in relation to environmental shear. *J. Atmos. Sci.*, **71**, 2713–2732, https://doi.org/10.1175/JAS-D-13-0298.1.

DeMaria, M., M. Mainelli, L. K. Shay, J. A. Knaff, and J. Kaplan, 2005: Further improvements to the Statistical Hurricane Intensity Prediction Scheme (SHIPS). *Wea. Forecasting*, **20**, 531–543, https://doi.org/10.1175/WAF862.1.

Eastin, M. D., W. M. Gray, and P. G. Black, 2005: Buoyancy of convective vertical motions in the inner core of intense hurricanes. Part II: Case studies. *Mon. Wea. Rev.*, **133**, 209–227, https://doi.org/10.1175/MWR-2849.1.

Emanuel, K. A., 1986: An air–sea interaction theory for tropical cyclones. Part I: Steady-state maintenance. *J. Atmos. Sci.*, **43**, 585–605, https://doi.org/10.1175/1520-0469(1986)043<0585:AASITF>2.0.CO;2.

Fang, J., and F. Zhang, 2011: Evolution of multiscale vortices in the development of Hurricane Dolly (2008). *J. Atmos. Sci.*, **68**, 103–122, https://doi.org/10.1175/2010JAS3522.1.

Fischer, M. S., R. F. Rogers, and P. D. Reasor, 2020: The rapid intensification and eyewall replacement cycles of Hurricane Irma (2017). *Mon. Wea. Rev.*, **148**, 981–1004, https://doi.org/10.1175/MWR-D-19-0185.1.

Gu, J.-F., Z.-M. Tan, and X. Qiu, 2016: Quadrant-dependent evolution of low-level tangential wind of a tropical cyclone in the shear flow. *J. Atmos. Sci.*, **73**, 1159–1177, https://doi.org/10.1175/JAS-D-15-0165.1.

Hazelton, A. T., R. F. Rogers, and R. E. Hart, 2017a: Analyzing simulated convective bursts in two Atlantic hurricanes. Part I: Burst formation and development. *Mon. Wea. Rev.*, **145**, 3073–3094, https://doi.org/10.1175/MWR-D-16-0267.1.

——, R. E. Hart, and R. F. Rogers, 2017b: Analyzing simulated convective bursts in two Atlantic hurricanes. Part II: Intensity change due to bursts. *Mon. Wea. Rev.*, **145**, 3095–3117, https://doi.org/10.1175/MWR-D-16-0268.1.

Hendricks, E. A., M. T. Montgomery, and C. A. Davis, 2004: The role of "vortical" hot towers in the formation of Tropical Cyclone Diana (1984). *J. Atmos. Sci.*, **61**, 1209–1232, https://doi.org/10.1175/1520-0469(2004)061<1209:TROVHT>2.0.CO;2.

Hong, S.-Y., Y. Noh, and J. Dudhia, 2006: A new vertical diffusion package with an explicit treatment of entrainment processes. *Mon. Wea. Rev.*, **134**, 2318–2341, https://doi.org/10.1175/MWR3199.1.

Iacono, M. J., J. S. Delamere, E. J. Mlawer, M. W. Shephard, S. A. Clough, and W. D. Collins, 2008: Radiative forcing by

long-lived greenhouse gases: Calculations with the AER radiative transfer models. *J. Geophys. Res.*, **113**, D13103, https://doi.org/10.1029/2008JD009944.

Jiménez, P. A., J. Dudhia, J. F. González-Rouco, J. Navarro, J. P. Montávez, and E. García-Bustamante, 2012: A revised scheme for the WRF surface layer formulation. *Mon. Wea. Rev.*, **140**, 898–918, https://doi.org/10.1175/MWR-D-11-00056.1.

Jones, S. C., 1995: The evolution of vortices in vertical shear. I: Initially barotropic vortices. *Quart. J. Roy. Meteor. Soc.*, **121**, 821–851, https://doi.org/10.1002/qj.49712152406.

Kain, J. S., 2004: The Kain–Fritsch convective parameterization: An update. *J. Appl. Meteor.*, **43**, 170–181, https://doi.org/10.1175/1520-0450(2004)043<0170:TKCPAU>2.0.CO;2.

Kepert, J. D., 2001: The dynamics of boundary layer jets within the tropical cyclone core. Part I: Linear theory. *J. Atmos. Sci.*, **58**, 2469–2484, https://doi.org/10.1175/1520-0469(2001)058<2469:TDOBLJ>2.0.CO;2.

——, 2006: Observed boundary layer wind structure and balance in the hurricane core. Part II: Hurricane Mitch. *J. Atmos. Sci.*, **63**, 2194–2211, https://doi.org/10.1175/JAS3746.1.

——, 2013: How does the boundary layer contribute to eyewall replacement cycles in axisymmetric tropical cyclones? *J. Atmos. Sci.*, **70**, 2808–2830, https://doi.org/10.1175/JAS-D-13-046.1.

——, 2017: Time and space scales in the tropical cyclone boundary layer, and the location of the eyewall updraft. *J. Atmos. Sci.*, **74**, 3305–3323, https://doi.org/10.1175/JAS-D-17-0077.1.

——, and Y. Wang, 2001: The dynamics of boundary layer jets within the tropical cyclone core. Part II: Nonlinear enhancement. *J. Atmos. Sci.*, **58**, 2485–2501, https://doi.org/10.1175/1520-0469(2001)058<2485:TDOBLJ>2.0.CO;2.

——, J. Schwendike, and H. Ramsay, 2016: Why is the tropical cyclone boundary layer not "well mixed"? *J. Atmos. Sci.*, **73**, 957–973, https://doi.org/10.1175/JAS-D-15-0216.1.

Landsea, C. W., and J. L. Franklin, 2013: Atlantic hurricane database uncertainty and presentation of a new database format. *Mon. Wea. Rev.*, **141**, 3576–3592, https://doi.org/10.1175/MWR-D-12-00254.1.

Montgomery, M., M. Nicholls, T. Cram, and A. Saunders, 2006: A vortical hot tower route to tropical cyclogenesis. *J. Atmos. Sci.*, **63**, 355–386, https://doi.org/10.1175/JAS3604.1.

Morrison, H., G. Thompson, and V. Tatarskii, 2009: Impact of cloud microphysics on the development of trailing stratiform precipitation in a simulated squall line: Comparison of one- and two-moment schemes. *Mon. Wea. Rev.*, **137**, 991–1007, https://doi.org/10.1175/2008MWR2556.1.

NCEP, 2000: NCEP FNL Operational Model Global Tropospheric Analyses, continuing from July 1999. Research Data Archive at the National Center for Atmospheric Research, Computational and Information Systems Laboratory, Boulder CO, accessed 4 October 2017, https://doi.org/10.5065/D6M043C6.

Nguyen, L. T., and J. Molinari, 2015: Simulation of the downshear reformation of a tropical cyclone. *J. Atmos. Sci.*, **72**, 4529–4551, https://doi.org/10.1175/JAS-D-15-0036.1.

——, ——, and D. Thomas, 2014: Evaluation of tropical cyclone center identification methods in numerical models. *Mon. Wea. Rev.*, **142**, 4326–4339, https://doi.org/10.1175/MWR-D-14-00044.1.

——, R. F. Rogers, and P. D. Reasor, 2017: Thermodynamic and kinematic influences on precipitation symmetry in sheared tropical cyclones: Bertha and Cristobal (2014). *Mon. Wea. Rev.*, **145**, 4423–4446, https://doi.org/10.1175/MWR-D-17-0073.1.

Noh, Y., W. Cheon, S. Hong, and S. Raasch, 2003: Improvement of the K-profile model for the planetary boundary layer based on large eddy simulation data. *Bound.-Layer Meteor.*, **107**, 401–427, https://doi.org/10.1023/A:1022146015946.

Nolan, D. S., Y. Moon, and D. P. Stern, 2007: Tropical cyclone intensification from asymmetric convection: Energetics and efficiency. *J. Atmos. Sci.*, **64**, 3377–3405, https://doi.org/10.1175/JAS3988.1.

——, J. A. Zhang, and D. P. Stern, 2009a: Evaluation of planetary boundary layer parameterizations in tropical cyclones by comparison of in situ observations and high-resolution simulations of Hurricane Isabel (2003). Part I: Initialization, maximum winds, and the outer-core boundary layer. *Mon. Wea. Rev.*, **137**, 3651–3674, https://doi.org/10.1175/2009MWR2785.1.

——, ——, and ——, 2009b: Evaluation of planetary boundary layer parameterizations in tropical cyclones by comparison of in situ observations and high-resolution simulations of Hurricane Isabel (2003). Part II: Inner-core boundary layer and eyewall structure. *Mon. Wea. Rev.*, **137**, 3675–3698, https://doi.org/10.1175/2009MWR2786.1.

——, R. Atlas, K. T. Bhatia, and L. R. Bucci, 2013: Development and validation of a hurricane nature run using the joint OSSE nature run and the WRF model. *J. Adv. Model. Earth Syst.*, **5**, 382–405, https://doi.org/10.1002/jame.20031.

Ooyama, K., 1969: Numerical simulation of the life cycle of tropical cyclones. *J. Atmos. Sci.*, **26**, 3–40, https://doi.org/10.1175/1520-0469(1969)026<0003:NSOTLC>2.0.CO;2.

Pendergrass, A. G., and H. E. Willoughby, 2009: Diabatically induced secondary flows in tropical cyclones. Part I: Quasi-steady forcing. *Mon. Wea. Rev.*, **137**, 805–821, https://doi.org/10.1175/2008MWR2657.1.

Rappin, E. D., and D. S. Nolan, 2012: The effect of vertical shear orientation on tropical cyclogenesis. *Quart. J. Roy. Meteor. Soc.*, **138**, 1035–1054, https://doi.org/10.1002/qj.977.

Reasor, P. D., and M. D. Eastin, 2012: Rapidly intensifying Hurricane Guillermo (1997). Part II: Resilience in shear. *Mon. Wea. Rev.*, **140**, 425–444, https://doi.org/10.1175/MWR-D-11-00080.1.

——, R. Rogers, and S. Lorsolo, 2013: Environmental flow impacts on tropical cyclone structure diagnosed from airborne Doppler radar composites. *Mon. Wea. Rev.*, **141**, 2949–2969, https://doi.org/10.1175/MWR-D-12-00334.1.

Riemer, M., M. T. Montgomery, and M. E. Nicholls, 2010: A new paradigm for intensity modification of tropical cyclones: Thermodynamic impact of vertical wind shear on the inflow layer. *Atmos. Chem. Phys.*, **10**, 3163–3188, https://doi.org/10.5194/acp-10-3163-2010.

Rios-Berrios, R., C. A. Davis, and R. D. Torn, 2018: A hypothesis for the intensification of tropical cyclones under moderate vertical wind shear. *J. Atmos. Sci.*, **75**, 4149–4173, https://doi.org/10.1175/JAS-D-18-0070.1.

Rogers, R. F., P. Reasor, and S. Lorsolo, 2013: Airborne Doppler observations of the inner-core structural differences between intensifying and steady-state tropical cyclones. *Mon. Wea. Rev.*, **141**, 2970–2991, https://doi.org/10.1175/MWR-D-12-00357.1.

——, P. D. Reasor, and J. A. Zhang, 2015: Multiscale structure and evolution of Hurricane Earl (2010) during rapid intensification. *Mon. Wea. Rev.*, **143**, 536–562, https://doi.org/10.1175/MWR-D-14-00175.1.

——, J. A. Zhang, J. Zawislak, H. Jiang, G. R. Alvey III, E. J. Zipser, and S. N. Stevenson, 2016: Observations of the structure and evolution of Hurricane Edouard (2014) during intensity change. Part II: Kinematic structure and the distri-

bution of deep convection. *Mon. Wea. Rev.*, **144**, 3355–3376, https://doi.org/10.1175/MWR-D-16-0017.1.

Ryglicki, D. R., and R. E. Hart, 2015: An investigation of center-finding techniques for tropical cyclones in mesoscale models. *J. Appl. Meteor. Climatol.*, **54**, 825–846, https://doi.org/10.1175/JAMC-D-14-0106.1.

——, J. D. Doyle, Y. Jin, D. Hodyss, and J. H. Cossuth, 2018: The unexpected rapid intensification of tropical cyclones in moderate vertical wind shear. Part II: Vortex tilt. *Mon. Wea. Rev.*, **146**, 3801–3825, https://doi.org/10.1175/MWR-D-18-0021.1.

Shapiro, L. J., 1983: The asymmetric boundary layer flow under a translating hurricane. *J. Atmos. Sci.*, **40**, 1984–1998, https://doi.org/10.1175/1520-0469(1983)040<1984:TABLFU>2.0.CO;2.

——, and H. E. Willoughby, 1982: The response of balanced hurricanes to local sources of heat and momentum. *J. Atmos. Sci.*, **39**, 378–394, https://doi.org/10.1175/1520-0469(1982)039<0378:TROBHT>2.0.CO;2.

Sitkowski, M., and G. M. Barnes, 2009: Low-level thermodynamic, kinematic, and reflectivity fields of Hurricane Guillermo (1997) during rapid intensification. *Mon. Wea. Rev.*, **137**, 645–663, https://doi.org/10.1175/2008MWR2531.1.

Skamarock, W. C., and Coauthors, 2008: A description of the Advanced Research WRF version 3. NCAR Tech. Note NCAR/TN-475+STR, 113 pp., https://doi.org/10.5065/D68S4MVH.

Smith, R. K., and M. T. Montgomery, 2016: The efficiency of diabatic heating and tropical cyclone intensification. *Quart. J. Roy. Meteor. Soc.*, **142**, 2081–2086, https://doi.org/10.1002/qj.2804.

——, ——, and N. Van Sang, 2009: Tropical cyclone spin-up revisited. *Quart. J. Roy. Meteor. Soc.*, **135**, 1321–1335, https://doi.org/10.1002/qj.428.

——, J. A. Zhang, and M. T. Montgomery, 2017: The dynamics of intensification in a Hurricane Weather Research and Forecasting simulation of Hurricane Earl (2010). *Quart. J. Roy. Meteor. Soc.*, **143**, 293–308, https://doi.org/10.1002/qj.2922.

Tewari, M., and Coauthors, 2004: Implementation and verification of the unified Noah land surface model in the WRF model. *20th Conf. on Weather Analysis and Forecasting/16th Conf. on Numerical Weather Prediction*, Seattle, WA, Amer. Meteor. Soc., 14.2a, https://ams.confex.com/ams/84Annual/techprogram/paper_69061.htm.

Vigh, J. L., and W. H. Schubert, 2009: Rapid development of the tropical cyclone warm core. *J. Atmos. Sci.*, **66**, 3335–3350, https://doi.org/10.1175/2009JAS3092.1.

Williams, G. J. J., 2015: The effects of vortex structure and vortex translation on the tropical cyclone boundary layer wind field. *J. Adv. Model. Earth Syst.*, **7**, 188–214, https://doi.org/10.1002/2013MS000299.

——, 2019: Idealized simulations of the inner core boundary layer structure in a landfalling tropical cyclone. Part I: Kinematic structure. *Trop. Cyclone Res. Rev.*, **8**, 47–67, https://doi.org/10.1016/j.tcrr.2019.07.006.

Wu, D., F. Zhang, X. Chen, A. Ryzhkov, K. Zhao, M. R. Kumjian, X. Chen, and P.-W. Chan, 2021: Evaluation of microphysics schemes in tropical cyclones using polarimetric radar observations: Convective precipitation in an outer rainband. *Mon. Wea. Rev.*, **149**, 1055–1068, https://doi.org/10.1175/MWR-D-19-0378.1.

Zeng, Z., Y. Wang, and L. Chen, 2010: A statistical analysis of vertical shear effect on tropical cyclone intensity change in the North Atlantic. *Geophys. Res. Lett.*, **37**, L02802, https://doi.org/10.1029/2009GL041788.

Zhang, F., and K. Emanuel, 2016: On the role of surface fluxes and WISHE in tropical cyclone intensification. *J. Atmos. Sci.*, **73**, 2011–2019, https://doi.org/10.1175/JAS-D-16-0011.1.

Zhang, J. A., and R. F. Rogers, 2019: Effects of parameterized boundary layer structure on hurricane rapid intensification in shear. *Mon. Wea. Rev.*, **147**, 853–871, https://doi.org/10.1175/MWR-D-18-0010.1.

——, ——, D. S. Nolan, and F. D. J. Marks, 2011: On the characteristic height scales of the hurricane boundary layer. *Mon. Wea. Rev.*, **139**, 2523–2535, https://doi.org/10.1175/MWR-D-10-05017.1.

——, ——, P. D. Reasor, E. W. Uhlhorn, and F. D. J. Marks, 2013: Asymmetric hurricane boundary layer structure from dropsonde composites in relation to the environmental vertical wind shear. *Mon. Wea. Rev.*, **141**, 3968–3984, https://doi.org/10.1175/MWR-D-12-00335.1.

——, ——, and V. Tallapragada, 2017: Impact of parameterized boundary layer structure on tropical cyclone rapid intensification forecasts in HWRF. *Mon. Wea. Rev.*, **145**, 1413–1426, https://doi.org/10.1175/MWR-D-16-0129.1.